

The Mina Justa Iron Oxide-Copper-Gold (IOCG) Deposit, Peru: Constraints on Metal and Ore Fluid Sources

Maria A. Rodriguez-Mustafa,^{1,†} Adam C. Simon,¹ Laura D. Bilenker,² Ilya Bindeman,³ Ryan Mathur,⁴ and Edson L. B. Machado⁵

¹ Department of Earth and Environmental Sciences, University of Michigan, 1100 North University Ave, Ann Arbor, Michigan 48109-1005, USA

² Department of Geosciences, College of Sciences and Mathematics, Auburn University, 2050 Beard Eaves Memorial Coliseum, Auburn, Alabama 36849, USA

Department of Geological Sciences, University of Oregon, 1275 E 13th Ave, Eugene, Oregon 97403-1272, USA
 Juniata College, 1700 Moore St, Huntingdon, Pennsylvania 16652, USA
 Marcobre, Jr. Lorenzo Bernini 149, Oficina 301, San Borja, Lima, Peru

Abstract

Iron oxide-copper-gold (IOCG) deposits are major sources of Cu, contain abundant Fe oxides, and may contain Au, Ag, Co, rare earth elements (REEs), U, and other metals as economically important byproducts in some deposits. They form by hydrothermal processes, but the source of the metals and ore fluid(s) is still debated. We investigated the geochemistry of magnetite from the hydrothermal unit and manto orebodies at the Mina Justa IOCG deposit in Peru to assess the source of the iron oxides and their relationship with the economic Cu mineralization. We identified three types of magnetite: magnetite with inclusions (type I) is only found in the manto, is the richest in trace elements, and crystallized between 459° and 707°C; type Dark (D) has no visible inclusions and formed at around 543°C; and type Bright (B) has no inclusions, has the highest Fe content, and formed at around 443°C. Temperatures were estimated using the Mg content in magnetite. Magnetite samples from Mina Justa yielded an average δ^{56} Fe $\pm 2\sigma$ value of 0.28 $\pm 0.05\%$ (n = 9), an average δ^{18} O $\pm 2\sigma$ value of $2.19 \pm 0.45\%$ (n = 9), and Δ^{17} O values that range between -0.075 and -0.047%. Sulfide separates yielded δ^{65} Cu values that range from -0.32 to -0.09%. The trace element compositions and textures of magnetite, along with temperature estimations for magnetite crystallization, are consistent with the manto magnetite belonging to an iron oxide-apatite (IOA) style mineralization that was overprinted by a younger, structurally controlled IOCG event that formed the hydrothermal unit orebody. Altogether, the stable isotopic data fingerprint a magmatic-hydrothermal source for the ore fluids carrying the Fe and Cu at Mina Justa and preclude significant input from meteoric water and basinal brines.

Introduction

Iron oxide-copper-gold (IOCG) mineral deposits are found worldwide and have a wide age range spanning from the Archean to the Cretaceous. These deposits are enriched in Fe and Cu, and can contain economically important amounts of Au, Ag, Co, U, and rare earth elements (REEs). They contain abundant magnetite and/or hematite, are structurally and/or stratigraphically controlled, and are usually associated with extensive Na-Ca alteration and more localized K alteration (Hitzman et al., 1992; Hitzman, 2000; Williams et al., 2005; Groves et al., 2010; Barton, 2014; Corriveau et al., 2016). It is generally accepted that IOCG deposits form by hydrothermal processes. However, the source of metals and ore fluid(s) remains controversial. Hitzman et al. (1992) and Pollard (2006) suggested a fluid of magmatic origin. Barton and Johnson (1996) proposed that a basinal brine would leach metals from the country rocks. Others have argued that IOCG deposits can be formed by a mix of both types of fluids (Hitzman et al., 1992; Hitzman, 2000; Chiaradia et al., 2006; Groves et al., 2010; Rieger and Marschik, 2012). At the Raúl-Condestable and Mina Justa IOCG deposits in Peru and the Candelaria IOCG deposit in Chile, sulfur isotope data indicate mixing of a magmatic fluid with a later, external fluid

†Corresponding author: e-mail, maalromu@umich.edu

source (seawater or brine). However, mixing with the external fluid is not required for ore deposition (de Haller and Fontboté, 2009; Li et al., 2018; del Real et al., 2020).

Based on the spatial and temporal relationship between iron oxide-apatite (IOA) and IOCG deposits in Chile, it has been suggested that in this region IOCG deposits might represent the shallower, lower-temperature manifestations of IOA deposits (Espinoza et al., 1996; Naslund et al., 2002; Sillitoe, 2003; Knipping et al., 2015a; Reich et al., 2016; Barra et al., 2017; Simon et al., 2018).

Rodriguez-Mustafa et al. (2020) showed that in the Candelaria IOCG deposit in Chile, the transition from shallower IOCG mineralization to a deeper IOA mineral assemblage is recorded by the geochemistry of magnetite. In Peru, several IOA and IOCG occurrences, including important deposits such as Raúl-Condestable, Marcona, and Mina Justa, show a similar spatial distribution to the deposits found in Chile (Atkin et al., 1985; Clark et al., 1990; Vidal et al., 1990; Hawkes et al., 2002; Injoque, 2002; de Haller et al., 2006; de Haller and Fontboté, 2009; Chen et al., 2010; Fig. 1a), but no genetic link between IOA and IOCG deposits has been established there yet.

In this study, we characterized magnetite from drill core samples from the Mina Justa IOCG deposit in Peru to assess the source of the iron oxides and their relationship with the

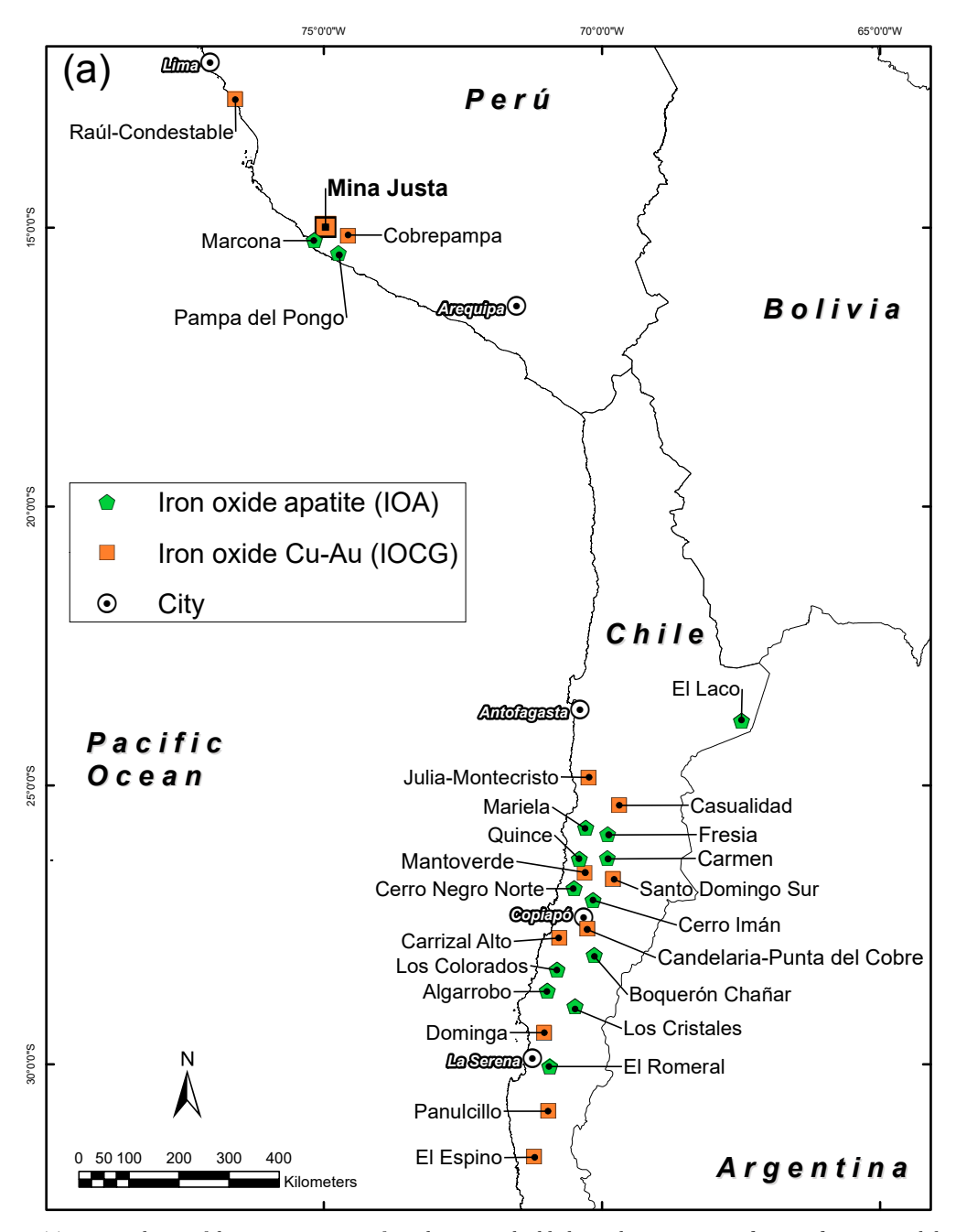


Fig. 1. (a). Regional map of the western margin of South America highlighting the main IOA and IOCG deposits in Chile and Peru. (b). Simplified geological map (at 1:7500 scale) of the Mina Justa deposit with the location of the sampled drill cores. Coordinate system: WGS84, UTM Zone 18L. The manto is hosted in and follows the bedding of the volcanosedimentary Río Grande Formation. The porphyritic andesitic dikes are postmineralization, structurally controlled features. (Map provided by Marcobre). The cross sections are shown in the Appendix (Figs. A1–A5).

economic Cu mineralization to better understand the evolution of the deposit. We investigated the textures and chemistry of magnetite by using a scanning electron microscope (SEM) and an electron probe microanalyzer (EPMA) to constrain the conditions under which magnetite formed, and we used the Mg content of magnetite grains to calculate magnetite crystallization temperatures. Furthermore, we measured Fe and O stable isotope abundances in magnetite, Cu isotope abundances in sulfides, and O and H isotope abundances in actinolite to fingerprint the source of the metals and ore fluids

and to evaluate the potential input of meteoric and basinal fluids in the mineralization process.

Geologic Background

The Mina Justa IOCG deposit is located within the IOA-IOCG belt in southern Peru, about 5 km northwest of the Marcona IOA deposit described by Chen et al. (2010; Fig. 1a). Basement rocks in the area consist of high-grade metamorphic rocks from the Paleo-Mesoproterozoic Arequipa Massif (Atkin et al., 1985; Wasteneys et al., 1995). The basement

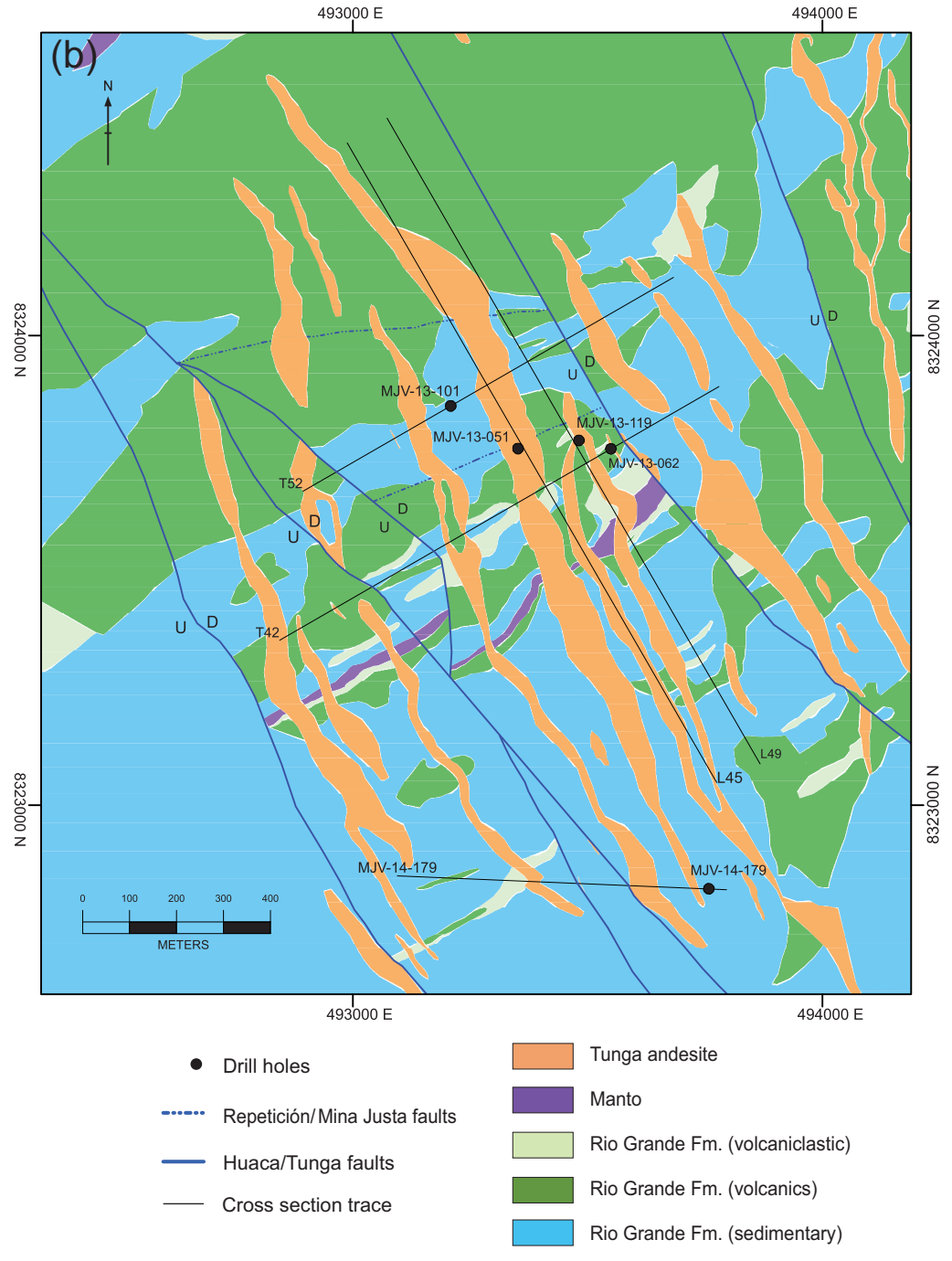


Fig. 1. (Cont.)

is overlain by a Paleozoic metasedimentary sequence that includes the Marcona Formation, which hosts most of the Fe mineralization in the Marcona IOA deposit (Hawkes et al., 2002; Injoque, 2002; Chen et al., 2010). The overlying Mesozoic volcanosedimentary sequence comprises the Río Grande, Jahuay, Yauca, and Copará Formations (Caldas Vidal, 1978). The Mina Justa deposit is hosted in the upper member of the ~4,000-m-thick Río Grande Formation, which dips 40° to 60° to the northwest, and is composed mainly of intercalations of porphyritic andesites, andesitic volcaniclastic rocks, fossiliferous limestones, arkoses, and mudstones (Caldas Vidal, 1978;

Chen et al., 2010). A recently identified diorite intrudes the Rio Grande Formation in the mine area. The Tunga Andesite Unit contains several 20- to 50-m-thick postmineralization porphyritic andesitic dikes with glomerophyric plagioclase crystals that cut the Río Grande Formation and the diorite and are referred to as ocöites due to their similarity to the Ocoa Formation near Copiapó, Chile (Hawkes et al., 2002; Chen et al., 2010).

The NW-trending Treinta Libras fault system is the major regional structure (Injoque, 2002) and, locally, the main fault systems in the area are Repetición/Mina Justa and Huaca/

Tunga (Hawkes et al., 2002; Fig. 1b). The Repetición faults developed in the Jurassic as a result of compression and sinistral shearing of the Treinta Libras fault system and are older than Cu mineralization at Mina Justa (Chen et al., 2010). They controlled the emplacement of the magnetite mantos at Marcona (Chen et al., 2010), and could have controlled the magnetite mantos at Mina Justa as well (Fonseca, 2016). The Mina Justa normal faults are interpreted to represent a reactivation of the Repetición faults due to a change to dextral transtension of the Treinta Libras fault system (Chen et al., 2010). The Huaca/Tunga normal faults were a major structural control for the SE-dipping main orebody that hosts most of the Cu mineralization (Hawkes et al., 2002). They are the youngest faults, and the porphyritic andesitic dikes in the area follow their orientation (Hawkes et al., 2002; Chen et al., 2010). Displacements in these dikes caused by faults from all systems evidence a more recent reactivation of all of them (Fonseca, 2016).

The Mina Justa deposit has a combined measured, indicated, and inferred oxide resource of 219 Mt at 0.51% Cu and sulfide resource of 213 Mt at 1.00% Cu, 8.0 g/t Ag, and 0.06 g/t Au (Fowler and Stephenson, 2016). The deposit consists of a main SE-plunging, structurally controlled orebody (Figs. 2, 3) dominated by magnetite, mushketovite, sulfides, and actinolite (± apatite) that occur as massive aggregates or as clasts and matrix in hydrothermal breccias (Fig. 4a, b). As the intensity of alteration commonly precludes the identification of primary lithologies within the orebody, and as textures vary between clearly breccia-hosted mineralization and wholesale replacement by hydrothermal minerals (where a breccia host cannot be confirmed), we use the term "hydrothermal unit" to reference intense replacement by hydrothermal minerals coincident with the main orebodies. The hydrothermal unit has the highest Cu grades in the deposit, but Cu mineralization is also hosted in the surrounding Río Grande Formation, presenting an outward zonation of hypogene sulfides from bornite-chalcocite (Fig. 4c) through chalcopyrite-bornite to chalcopyrite > pyrite (Fig. 4d, e) and to pyrite > chalcopyrite (Sillitoe, 2002; Hawkes, 2003). Fine-grained magnetite-dominated mantos (20 to 30 m thick) dip to the northwest (Figs. 1b, 2, 3), are parallel to bedding in the Río Grande Formation, and are interpreted to have replaced limestone-rich horizons in that unit (Fig. 4f-h; Sillitoe, 2002). They host localized Cu mineralization with similar sulfide assemblages as the main hydrothermal unit. The deposit hosts a supergene Cu oxide zone (chrysocolla, atacamite) that extends on average to 200 m below the surface (Chen et al., 2010).

A 7-stage paragenetic sequence for the Mina Justa deposit was presented by Chen et al. (2010). Those authors described an early-stage massive magnetite body, associated with microcline (Ar/Ar 142.4 \pm 6.7 Ma) and crosscut by actinolite (Ar/Ar 110.9 \pm 0.7 Ma), and younger main and upper bodies consisting of magnetite-pyrite (associated with microcline, Ar/Ar 103.7 \pm 0.6 and 101.5 \pm 0.7 Ma). The magnetite-pyrite bodies host most of the overprinting Cu mineralization (microcline envelopes, Ar/Ar 99.1 \pm 0.9 and 95.0 \pm 0.6 Ma), but Cu sulfides also overprint the massive magnetite body. In our study, the massive magnetite body corresponds to the NW-dipping manto and the magnetite-pyrite bodies relate

to the hydrothermal unit. Chen et al. (2010) presented and used geochronological data to conclude that the manto is a distinct, older event (probably associated with the formation of the neighboring Marcona IOA deposit) and is not related to the IOCG mineralization hosted in the Mina Justa hydrothermal unit. However, the Cu mineralization hosted in the manto belongs to the same mineralizing event identified in the hydrothermal unit (Sillitoe, 2002).

More recently, Hu et al. (2020) summarized the paragenesis of the hydrothermal unit orebody into 4 stages: 1) magnetiteactinolite-K-feldspar-albite ± apatite early alteration stage; 2) hematite stage; 3) magnetite + pyrite ± titanite ± quartz ± chlorite stage that includes mushketovite (specular hematite from stage 2 that has been converted to magnetite retaining the original morphology) and granular magnetite; 4) copper mineralization stage dominated by chalcopyrite and other copper sulfides (bornite, chalcocite, and digenite) that incorporate Ag in their structure and occur as veins cutting the previous stages (Chen et al., 2010). Chalcopyrite partially or completely replaces pyrite from stage 3 (Chen et al., 2010; Li et al., 2018; Figs. 4a, 3d), occurs with chalcocite and bornite (Fig. 5b, c), and presents rims of covellite (Fig. 5d). Hematite coexists with bornite and chalcocite, which present symplectitic textures (Fig. 5e). Minor, later sphalerite-galena, calcitequartz (Fig. 4e), and hematite (Fig. 5c) are present as veins or filling cracks (Chen et al., 2010).

Hu et al. (2020) studied stage 3 magnetite and mushketovite from the hydrothermal unit and concluded that they formed from a cooling hydrothermal fluid. For the same stage, Chen et al. (2011) reported δ^{18} O values for magnetite (2.7 to 4.7%) and δ^{34} S values for pyrite (1.1 and 1.6%), and interpreted those as being associated with a magmatic fluid. The authors also reported results of thermometry on fluid inclusions of unknown origin in quartz from stage 3 and calcite from stage 4, and inferred that external fluids were involved in the Cu mineralization. Furthermore, Li et al. (2018) reported in-situ δ^{34} S values and Co/Ni and Se/S ratios of stage 3 pyrite (-0.5 to 6.4‰) and stage 4 chalcopyrite (-0.6 to 4.6‰). The authors concluded that the fluids involved in stage 3 were primarily magmatic with an incursion of a later, external fluid, whereas the fluids for stage 4 were mainly external fluids that leached metals from the andesitic host rocks, but they do not rule out input from magmatic fluids in this stage.

Methods

Sample collection

We selected 19 core samples from five drill holes (Table 1) to investigate the lateral and vertical variations in the geochemistry of the mineralization in the Mina Justa deposit (Fig. 1b; App. Figs. A1–A5). The samples come from between 87 m and 472 m downhole to avoid the Cu oxide zone and are classified as coming from the manto or the hydrothermal unit.

Sample preparation

The samples from Mina Justa were either mounted in epoxy resin or sent for thin section fabrication in order to perform EPMA and SEM analyses on polished grains. For isotopic analyses, nine representative samples of magnetite and six

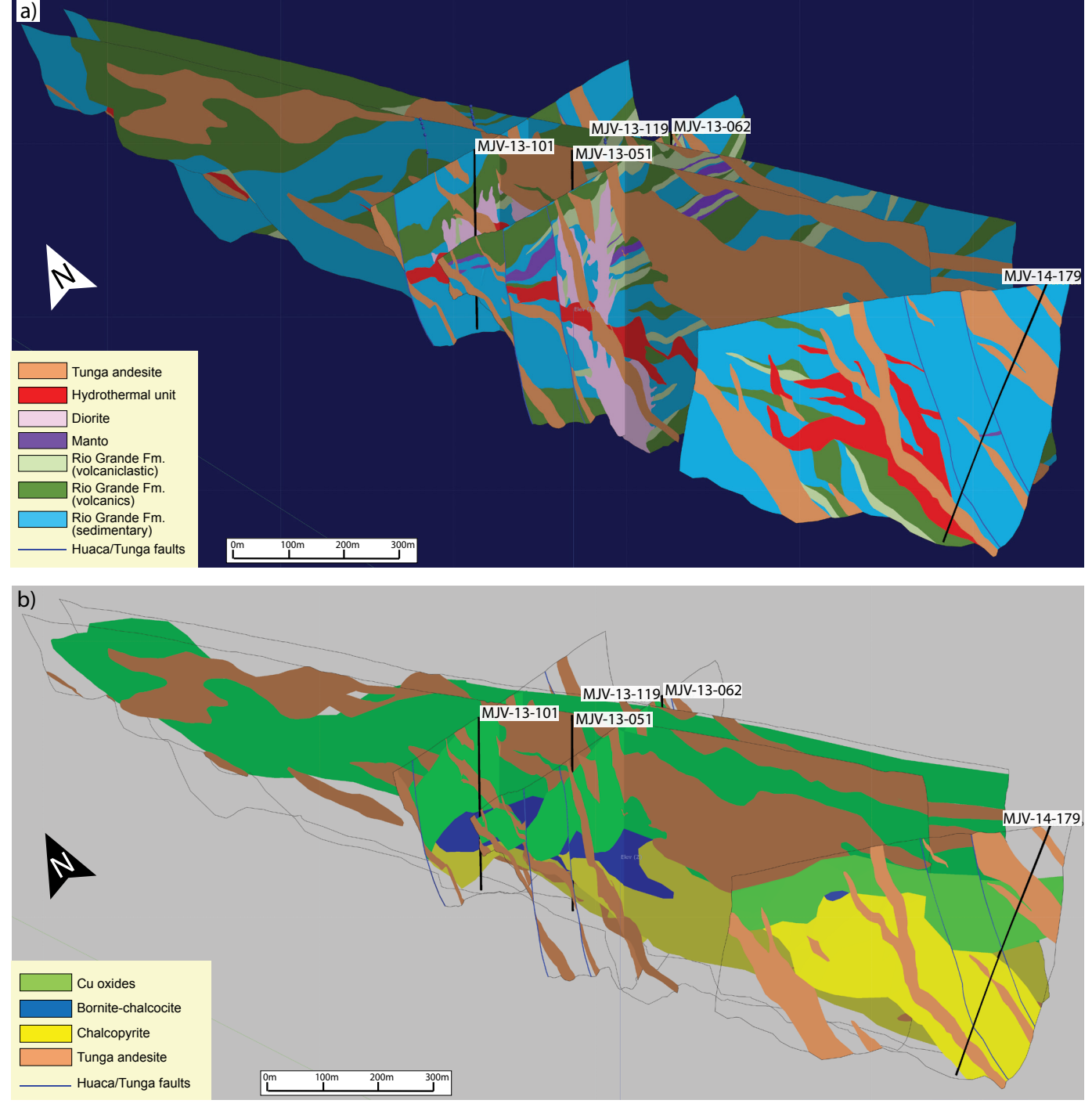


Fig. 2. Perspective view of sections and drill traces in a 3-D model of the Mina Justa deposit highlighting the longitudinal sections. The manto ore body dips to the northwest while the structurally controlled hydrothermal unit dips to the southeast. The black lines correspond to the sampled drill holes. a) Distribution of lithological units. b) Distribution of Cu mineralization. (Diagrams provided by Marcobre).

representative samples of sulfides (chalcopyrite, chalcocite, and bornite) from the hydrothermal unit and manto bodies were selected. Each sample was crushed using an agate mortar and pestle, which was rinsed with ethanol and put through an ultrasonic cleaner between each sample to prevent contamination. The magnetic fraction was obtained by using a hand magnet wrapped in weighing paper, and individual, visibly

unweathered magnetite/mushketovite and sulfide grains were handpicked using a binocular microscope at ~40× magnification. Actinolite separates were obtained from two samples by using a Frantz magnetic separator and handpicking individual grains under the microscope to eliminate the presence of other mineral phases. Aliquots of actinolite and magnetite analyzed for O isotopes, described below, were prefluorinated

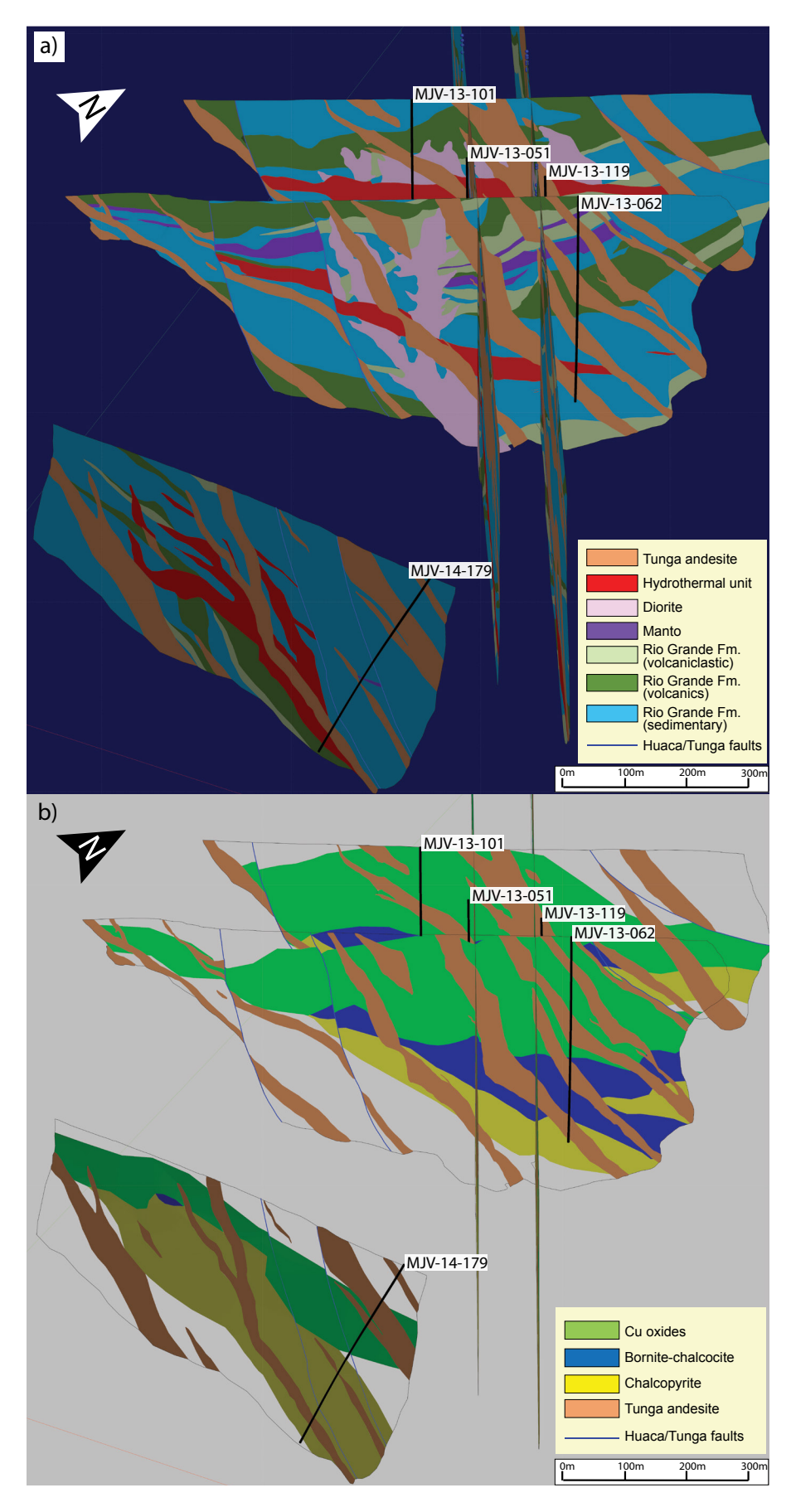


Fig. 3. Perspective view of sections and drill traces in a 3-D model of the Mina Justa deposit highlighting the transverse sections. The manto ore body dips to the northwest while the structurally controlled hydrothermal unit dips to the southeast. The black lines correspond to the sampled drill holes.

a) Distribution of lithological units. b) Distribution of Cu mineralization. (Diagrams provided by Marcobre).

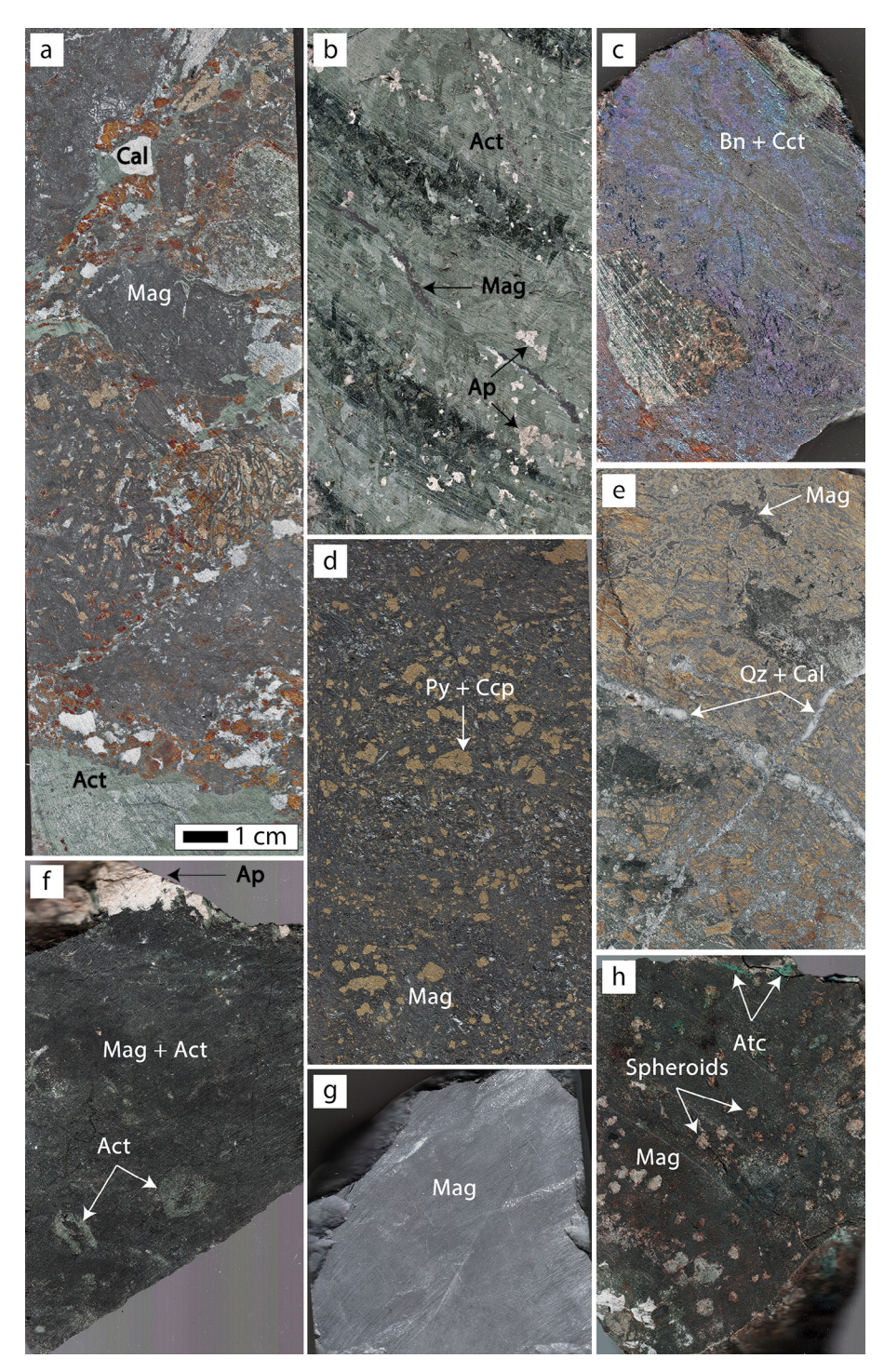


Fig. 4. Representative hand samples from the Mina Justa deposit. Samples a-e come from the hydrothermal unit, and samples f-h from the manto. All samples have the same scale (Fig. 4a). Act = actinolite, Ap = apatite, Atc = atacamite, Bn = bornite, Cal = calcite, Cct = chalcocite, Mag = magnetite, Qz = quartz. (a) Sample GM13: Hydrothermal unit. Hydrothermal breccia with clasts of magnetite, actinolite, calcite, and altered host rock in a magnetite (mushketovite) and mixed sulfide matrix. (b) Sample NN58: Massive actinolite intergrown with apatite, crosscut by magnetite veinlets. (c) Sample NN53: Sample from the sulfide mineralization in the hydrothermal unit. Bornite and chalcocite in magnetite matrix with an altered volcanic clast. (d) Sample NN06: Massive magnetite (mushketovite) with disseminated chalcopyrite replacing pyrite. (e) Sample NN16: Hydrothermal breccia with magnetite-chloritized actinolite matrix with quartz, apatite, and pyrite clasts. Most of the pyrite has been replaced by chalcopyrite, galena, and sphalerite. Quartz-calcite veins crosscut the breccia. (f) Sample NN50: Fine grained magnetite and actinolite. The latter is also replacing marine fossils. Part of a later apatite, fibrous actinolite, and mushketovite vein is visible in the top. (g) Sample NN52: Very fine-grained, massive magnetite. (h) Sample NN04: Fine-grained magnetite matrix with spheroids composed of calcite, quartz, and potassium feldspar. The spheroids are surrounded by a coarser magnetite halo. Supergene atacamite replacing covellite is also present.

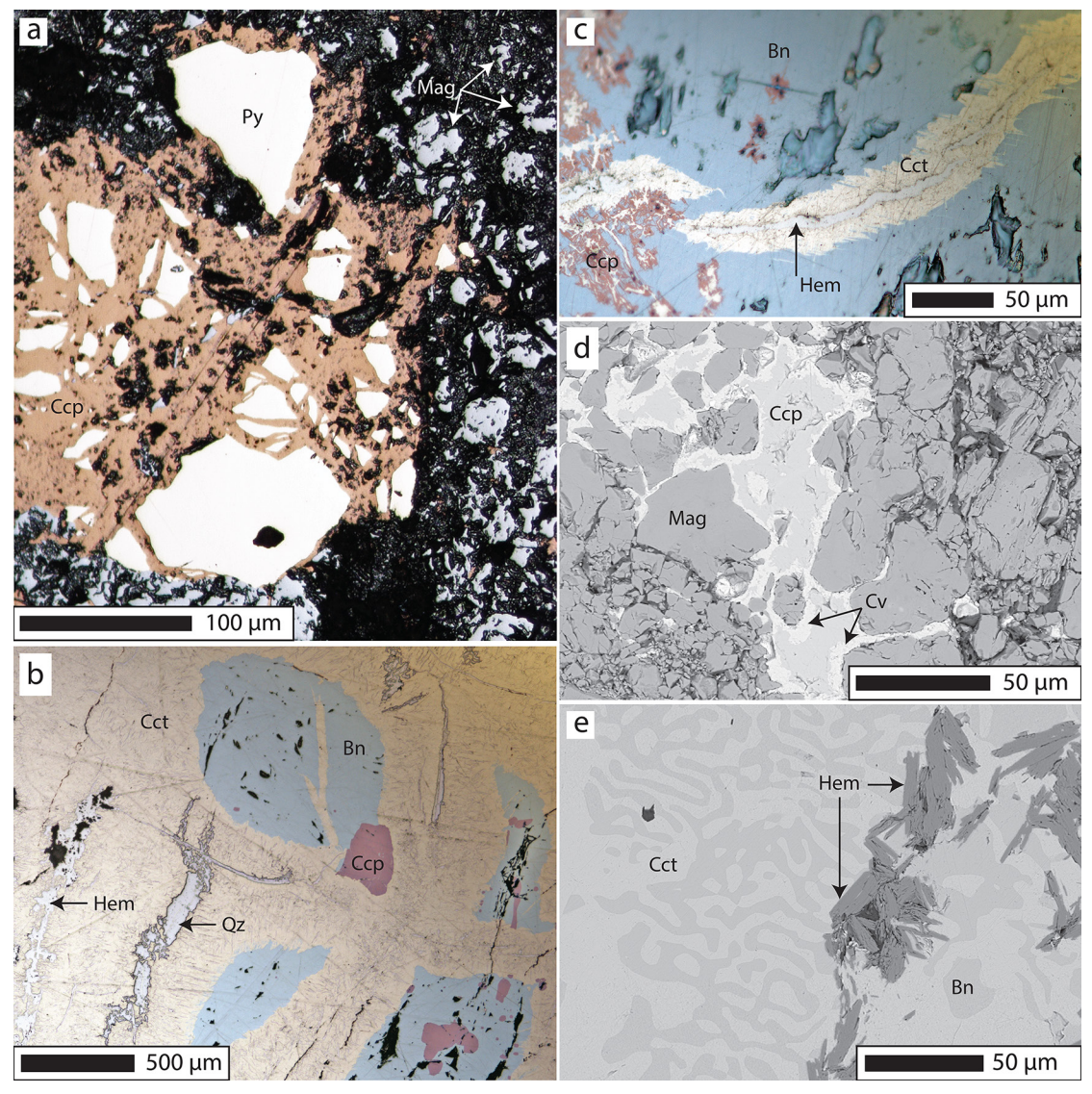


Fig. 5. Reflected light photographs (a-c) and backscattered electron (BSE) images (d-e) of: (a) Disseminated magnetite and chalcopyrite replacing pyrite (sample NN59). (b) Chalcocite, which exhibits flame texture, is replacing bornite. The latter is replacing chalcopyrite. Hematite and quartz are also present filling interstices and fractures (sample NN51). (c) Lateral slip en echelon hematite vein that resulted from local extension. The vein has a chalcocite halo replacing bornite (Sample NN01). (d) Massive magnetite grains with interstitial chalcopyrite with covellite rims (sample NN06). (e) Hematite coexisting with chalcocite and bornite that display a symplectitic texture (sample NN53). Abbreviations: Bn = bornite, Cct = chalcocite, Ccp = chalcopyrite, Hem = hematite, Mag = magnetite, Py = pyrite, Qz = quartz.

for 4 h to remove impurities and alteration products such as chlorite and other reactive phases.

EPMA and FE-SEM

Backscattered electron (BSE) images and energy dispersive X-ray spectroscopy (EDS) maps were obtained to characterize textures and elemental variations by using a JEOL 7800FLV field emission-scanning electron microscope (FE-SEM) in the Electron Microbeam Analysis Laboratory at the University of Michigan. In the same facility, point and line transect analyses were performed by using a Cameca SX-100 electron microprobe with a focused beam, a voltage of 20 keV, and a current of 40 nA for magnetite grains. Counting times, standards, and detection limits are listed in the Appendix

(Table A6). We measured Mg, Al, Si, Ca, Ti, V, Cr, Mn, Co, Ni, and Fe in magnetite grains and carefully avoided inclusions. We executed TiK α -VK β and FeK α -CoK β interference corrections.

Iron isotopes

To obtain pure Fe from each sample, dissolution and ion chromatography were performed on magnetite/mushketovite grains. Approximately 2.0 mg of sample were digested in HF and HNO₃ for ≥24 h, dried on a hot plate, refluxed in aqua regia, and dried once more to completely dissolve each sample. In preparation for column chemistry, samples were dissolved in 0.5 mL 8N HCl, dried, and dissolved in 0.4 mL 8N HCl at ~120°C. The conditioning and elution

Table 1. Sample Details

Sample	Hole	$^{1}\mathrm{UTM}$ (E) zone 18L	1 UTM (N) zone 18L	Downhole depth (m)	Geologic unit
NN01	MV-13-051	493352	8323759	159.5	Manto
NN03	MV-13-051	493352	8323759	183.1	Hydrothermal unit
NN02	MV-13-051	493352	8323759	288.5	Hydrothermal unit
NN50	MV-13-062	493550	8323758	87.3	Manto
NN51	MV-13-062	493550	8323758	93.1	Manto
NN52	MV-13-062	493550	8323758	103.5	Manto
NN53	MV-13-062	493550	8323758	344.9	Hydrothermal unit
NN54	MV-13-062	493550	8323758	362	Hydrothermal unit
NN04	MV-13-101	493209	8323849	178	Manto
NN56	MV-13-119	493482	8323776	129	Manto
NN57	MV-13-119	493482	8323776	395.5	Hydrothermal unit
NN58	MV-13-119	493482	8323776	396	Hydrothermal unit
NN59	MV-13-119	493482	8323776	403.8	Hydrothermal unit
NN06	MV-14-179	493759	8322822	282.63	Hydrothermal unit
GM07	MV-14-179	493759	8322822	290.5	Hydrothermal unit
GM13	MV-14-179	493759	8322822	461.68	Hydrothermal unit
GM14	MV-14-179	493759	8322822	463.1	Hydrothermal unit
NN15	MV-14-179	493759	8322822	467.4	Hydrothermal unit
NN16	MV-14-179	493759	8322822	472.8	Hydrothermal unit

¹Coordinate system: WGS84

procedures were completed following the procedure of Huang et al. (2011) using Biorad AGI-X8 Ion Exchange Resin (200–400 mesh). All reactants (HNO₃, HCl, HF) were Optima Grade and H₂O was ultrapure. The stable Fe isotope analyses were performed at the Pacific Centre for Isotopic and Geochemical Research, University of British Columbia, using a Nu Plasma 1700 multi collector-inductively coupled plasma-mass spectrometer (MC-ICP-MS) in dry plasma mode with a DSN-100 Desolvating Nebulizer System. All analyses were performed in true high-resolution mode, and isobaric interferences (i.e., Ar complexes) were fully resolved from the Fe isotopes (54Fe, 56Fe, 57Fe). Minor Cr corrections were done online for each analysis by monitoring 52Cr. Every sample was measured between 3 and 6 times and was bracketed immediately before and after each analysis by the measurement of standard 14 from the Institute for Reference Materials and Measurements (IRMM-14). The concentration of Fe in the samples was adjusted to be within 10% of the bracketing standard solution. Analyses of the reference material BCR-2 yielded an average value of δ^{56} Fe 0.08 \pm 0.05‰ (n = 11), which is consistent with the value of $0.09 \pm 0.01\%$ (n = 8) recommended by Craddock and Dauphas (2011).

Oxygen and hydrogen isotopes

Oxygen isotope abundances (^{16}O and ^{18}O) of magnetite/mushketovite and actinolite separates (^{2}O – 2 .2 mg each) were measured at the University of Oregon using BrF₅ in a laser fluorination line connected to a Thermo-Finnigan MAT 253 gas isotope ratio mass spectrometer (IRMS) in dual inlet mode. Laser power was slowly increased to minimize jumping movements of the grains during fluorination with BrF₅. Yields (μ mol/mg of extracted O_2 gas) were monitored by a Baratron gauge. For samples that did not experience grain jumping, O_2 yields were close to the theoretical 100%, demonstrating that analyzed magnetite grains were not weathered. The Gore Mountain garnet (GMG, 6.52%) and San Carlos olivine (SCO, 5.25%) standards were measured prior to, during, and

after the sample analyses to quantify the data onto a standard mean ocean water (SMOW) scale (Loewen and Bindeman, 2016). Analyses of the standard GMG yielded $\delta^{18}\text{O} \pm 2\sigma$ values of 6.17 \pm 0.15% for the magnetite and actinolite samples. The analytical values were corrected to Vienna standard mean ocean water (VSMOW) scale by using the difference between the measured and the expected value for the standard for each day.

The abundance of ¹⁷O was measured in 4 magnetite samples and capital delta values were calculated using Equation 1:

$$\Delta^{17}O_{\text{sample}} = \delta^{17}O_{\text{sample}} - \delta^{18}O_{\text{sample}} \times 0.5305 \tag{1}$$

where 5.305 is the slope of the reference line for minerals formed at high temperatures (Pack et al., 2016; Sharp et al., 2018; Miller et al., 2020). Triple oxygen isotopes were measured in a single session with $\rm O_2$ gas as analyte run against calibrated reference gas, with an additional gas chromatographic purification step in a controlled He flow using a 6-ft-long zeolite column that was added to the University of Oregon fluorination line (Bindeman et al., 2018). This procedure is needed to minimize potential $^{17}\rm O$ contaminants such as NF and organics. The average San Carlos olivine during $\Delta^{17}\rm O$ analyses was $-0.05 \pm 0.012\%$ (2 σ , n=3).

The water content and stable δD isotope ratios of actinolite samples were measured over 2 days by thermal pyrolysis using a thermal conversion elemental analyzer attached to a MAT 253 IRMS by a continuous flow method also at the University of Oregon. We used a glassy carbon reactor held at 1,450°C, following the analytical procedures described in Bindeman et al. (2012). For standards, we used USGS57 biotite and USGS58 muscovite (Qi et al., 2017). Our analyses yielded average $\delta D \pm 2\sigma$ (n=10) values of -90.9 ± 2.5 and $-27.3 \pm 1.0\%$, and calculated wt % H₂O $\pm 2\sigma$ (n=10) contents of 2.5 ± 0.1 and $1.0 \pm 0.1\%$, respectively. Water was determined by peak integration of H and D areas relative to that of the standard NBS30 and USGS57 micas (nominal H₂O = 3.5 wt %). The results are reported relative to VSMOW.

Cu isotopes

Approximately 10 to 30 mg of Cu sulfide samples were hand separated. The samples were dissolved by 3 mL of heated ultrapure aqua regia. Solutions were dried and Cu was purified with the ion exchange chromatography described in Mathur et al. (2009). Solutions were measured at Rutgers University on the Neptune plus MC-ICP-MS in low resolution mode with a jet cone to enhance sensitivity. They were measured at 100 ppb Cu and generated 5V on the 63Cu. Mass bias was corrected for by standard sample bracketing. All values are reported as per mil relative to the NIST 976 standard. On peak, blank corrections were applied to each value, and the blank was measured eight times during each session. Samples and standards matched within 15% of the ⁶³Cu voltage. Samples were measured in duplicate and errors are within 0.08%, which is the 2σ variation of the NIST 976 throughout the measuring session. We assume 0.08‰ as the estimate for the error on all measurements. To verify the accuracy of the measurements, a U.S. penny from 1838 (first reported in Mathur et al., 2009) overlapped with the published value of δ^{65} Cu = 0.05 ± 0.06‰ (n = $\frac{1}{4}$).

Results

Magnetite textures

Magnetite and mushketovite (hematite that has been replaced by magnetite preserving the original tabular shape) occur as massive aggregates, disseminations, veins, and clasts. Actinolite is fine grained and intergrown with magnetite, or it is massive, fibrous and associated with apatite. The fibrous actinolite presents zonation in BSE and contains titanite inclusions.

Based on morphology, BSE grayscale tone and inclusion content, three main textures of Fe oxides were identified in the Mina Justa samples (Table 2). Magnetite with inclusions (type I) consists of cores in euhedral to subhedral magnetite grains and bands that contain numerous submicron-sized, rounded to elongated inclusions of titanite and a Ca-Mg silicate (probably actinolite; Fig. 6a-c). Type I magnetite presents a medium to dark tone in BSE and was only identified in the manto. Types Dark (D) and Bright (B) were identified in both the manto and the hydrothermal unit. Type D consists of patches in mushketovite (Fig. 6d, 7a) and in granular magnetite that present a dark tone in BSE images but no visible mineral inclusions (Fig. 7b-c). Type Bright (B) refers to the lighter BSE bands in mushketovite (Fig. 6d, 7a), patches in granular magnetite (Fig. 7b-c), and anhedral granular magnetite grains that are inclusion-free (Fig. 7d). In the manto, type B is also found meeting at triple junctions, surrounding type I magnetite grains (Fig. 6b-c), and locally associated with chlorite and interstitial titanite (Fig. 8). In the hydrothermal unit, mushketovite grains of type B are porous and contain scheelite inclusions (inset in Fig. 7a).

Trace element compositions of magnetite

The EPMA data are compiled in Appendix Table A7. Summary statistics of element concentrations for samples from the manto and the hydrothermal unit, as well as for each magnetite type, are presented in Table 3. Cobalt was below detection limit for more than 50% of the analyses, and no statistics for Co are reported.

All magnetite grains from the manto are enriched in Mn $(0.09 \pm 0.03 \text{ wt \%})$, Cr $(0.03 \pm 0.01 \text{ wt \%})$, V $(0.96 \pm 0.17 \text{ wt \%})$ wt %), and Ni (0.01 ± 0.01 wt %) with respect to magnetite from the hydrothermal unit (Mn $[0.05 \pm 0.02 \, \mathrm{wt} \, \%]$, Cr $[0.01 \pm$ 0.01 wt %], and V $[0.21 \pm 0.19 \text{ wt } \%]$; Fig. 9). Magnetite grains from the manto overlap with but are slightly depleted in Fe $(70.7 \pm 1.10 \text{ wt }\%)$ relative to the hydrothermal unit grains $(71.8 \pm 0.83 \text{ wt }\%)$, and magnetite type B is the richest in Fe in both the manto and the hydrothermal unit. Magnetite type I, only found in the manto, is also enriched in Si (0.97 ± 0.55 wt %), Mg (0.22 ± 0.15 wt %), Ti (0.11 ± 0.06 wt %), and Ca $(0.41 \pm 0.19 \text{ wt }\%)$ compared to types D (Si $[0.54 \pm$ 0.41 wt %], Mg [0.11 \pm 0.08 wt $\frac{1}{2}$], Ti [0.05 \pm 0.04 wt %], Ca $[0.19 \pm 0.16 \text{ wt }\%]$) and B (Si $[0.14 \pm 0.07 \text{ wt }\%]$, Mg $[0.03 \pm$ 0.04 wt %], Ti $[0.04 \pm 0.03]$, Ca $[0.04 \pm 0.07 \text{ wt }\%]$; Fig. 9). Aluminum is slightly enriched in type D magnetite grains in the hydrothermal unit but has a similar concentration in the other magnetite types.

Temperature estimations

We calculated formation temperatures of individual magnetite grains by implementing the Mg in magnetite empirical geothermometer (TMg - mag ($^{\circ}$ C) = -8344(± 320)/[lnXMg - $4.1(\pm 0.28)$] – 273) developed by Canil and Lacourse (2020). Where Mg was below detection limit, we used half of that value to estimate the minimum formation temperature, which corresponds to 371°C. The number of analyses below detection limit were 87 out of 195 for type B and nine out of 37 for type D. Table 3 provides the summary statistics for the temperatures for the manto, the hydrothermal unit, and the different magnetite types. Magnetite from the manto crystallized over a temperature range between 372° and 707°C, and magnetite from the hydrothermal unit crystallized over the range from 371° to 657°C. Magnetite types D and B have average ± 1sd estimated formation temperatures of 543° ± 106°C and 443° ± 74°C, respectively. The latter value is

Table 2: Magnetite Types and Their Estimated Temperatures by Using the Mg in Magnetite Geothermometer

Туре	Geologic unit	Visible inclusions	Equivalent type in Hu et al. 2020	Minimum temperature (°C)	Maximum temperature (°C)	Average temperature ($^{\circ}C \pm 1sd$)	n
Inclusion (I)	Manto	Yes	$\begin{array}{l} None \\ T_{M1}2,T_{M2}1 \\ T_{M1}3,T_{M2}2 \end{array}$	459	707	628 ± 95	8
Dark (D)	Manto and hydrothermal unit	None		373	705	543 ± 106	37
Bright (B)	Manto and hydrothermal unit	None		371 ¹	671	443 ± 74	195

¹Estimated as a function of half of the Mg detection limit; may impact the average temperature for this magnetite type Notes: *n* = number of points analyzed, sd = standard deviation

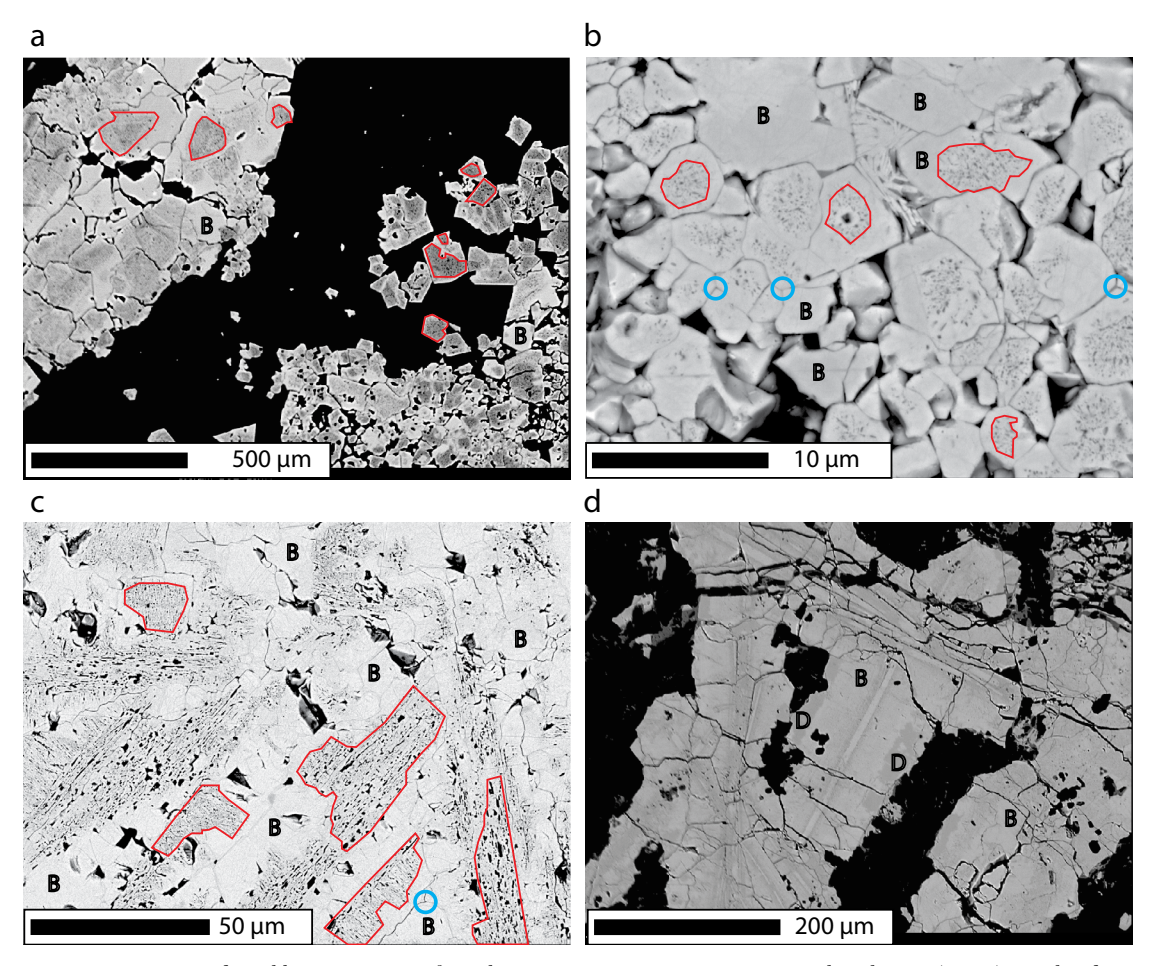


Fig. 6. Magnetite and mushketovite textures from the manto at Mina Justa. Magnetite with inclusions (type I) is outlined in red, and types Dark (D) and Bright (B) are identified with the letters D and B, respectively. Triple junctions are circled in blue. (a) Type I magnetite euhedral to subhedral cores surrounded by magnetite type B (sample NN51). (b) Another example of magnetite type B surrounding magnetite type I. Note the difference in scale with Fig. 6a. The submicron inclusions are visible only in magnetite type I. The platy mineral in the top center is hematite (sample NN01). (c) Type I magnetite bands containing elongated inclusions. Type B surrounds type I (sample NN01). (d) Mushketovite showing patches of magnetite types B and D. Type D magnetite shows a darker color in backscattered electron imaging (BSE), but no visible inclusions (sample NN04).

influenced by the number of analyses below the detection limit. The higher magnetite crystallization temperatures of the manto are associated with magnetite type I (not present in the hydrothermal unit), which records the highest temperatures (>700°C; Fig. 10) and has an average \pm 1sd estimated formation temperature of 628° \pm 95°C.

Hu et al. (2020) report that the process of reducing hematite to mushketovite produces a change of the crystal lattice of the latter, which results in the reequilibration of the new phase with the fluid so that the Mg content of mushketovite reflects the temperature at which mushketovite formed. We note that we chose spots for EPMA analysis to avoid inclusions visible in BSE. We recognize that this cannot eliminate inclusions that may have existed within the penetration volume of the electron beam, which is approximately 1,500 nm deep by 1,500 nm wide based on Monte Carlo simulations for the EPMA conditions reported above. The effect of Mgbearing inclusions will depend on the mass ratio of Mg inclusions to Mg in magnetite, which we cannot quantitatively

constrain. We scrutinized the magnetite compositional data and concluded that the model temperatures reported in our manuscript accurately reflect changes in the crystallization temperature among different generations of magnetite.

Iron isotope compositions of magnetite separates

Iron isotope data for magnetite samples are summarized in Table 4. The δ^{56} Fe \pm 2 σ values relative to the IRMM-14 standard for magnetite from Mina Justa range between 0.17 \pm 0.03 and 0.40 \pm 0.10% $_{o}$ and yield an average value of 0.28 \pm 0.05% $_{o}$ (n = 9).

Oxygen and hydrogen isotope compositions of magnetite and actinolite separates

Oxygen isotope data for magnetite and actinolite are summarized in Table 4. The $\delta^{18}O \pm 2\sigma$ values for magnetite from Mina Justa range between 0.74 \pm 0.15 and 3.16 \pm 0.15‰ and have an average $\delta^{18}O \pm 2\sigma$ value of 2.19 \pm 0.45‰ (n = 9). The $\Delta^{17}O$ values from 4 magnetite samples range between –0.075

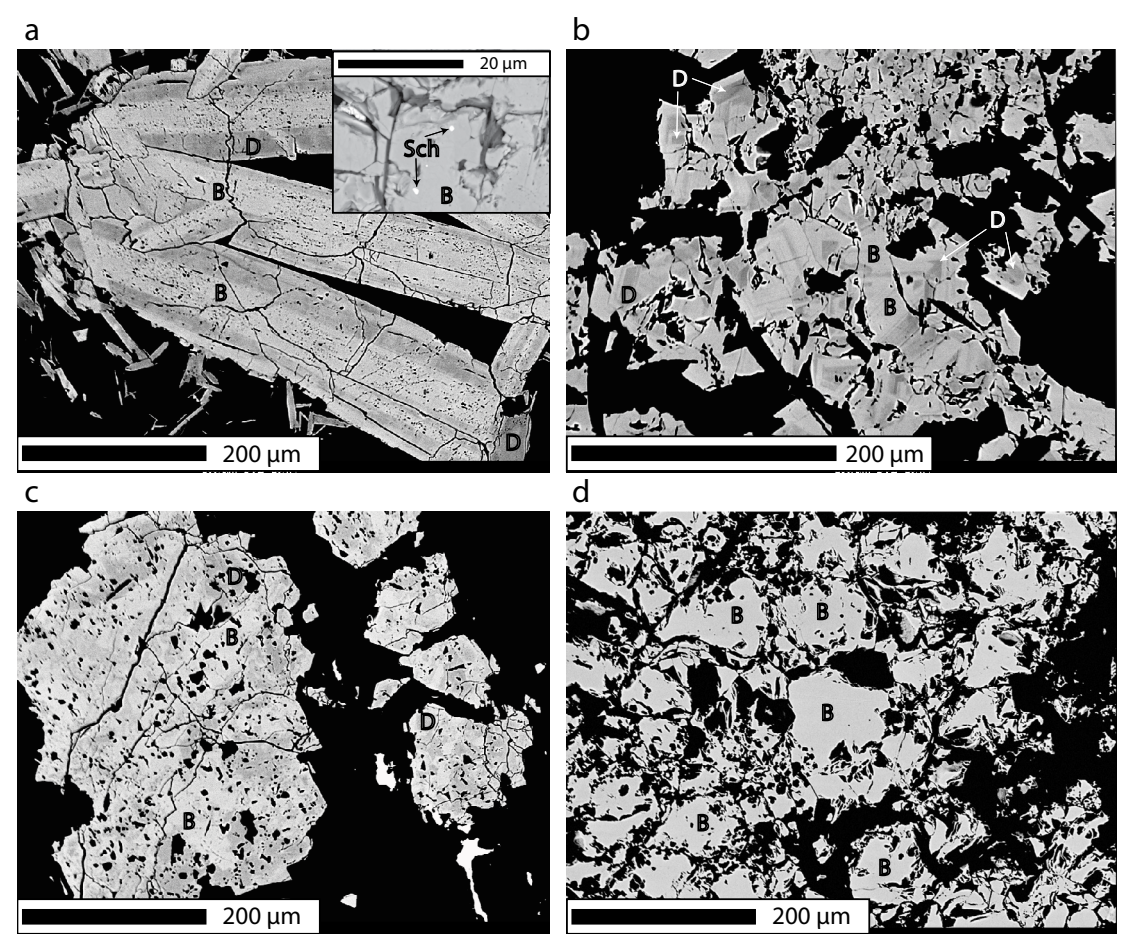


Fig. 7. Magnetite and mushketovite textures from the hydrothermal unit at Mina Justa. Magnetite types Dark (D) and Bright (B) are identified with the letters D and B, respectively. (a) Mushketovite showing patches of magnetite types B and D. Type D magnetite shows a darker color in backscattered electron imaging (BSE), but no visible inclusions. Type B is porous and has scheelite inclusions (Sch in inset; sample NN54). (b) Granular magnetite showing zoning of magnetite types D and B (sample NN57). (c) Fractured granular magnetite with patches of type D and B magnetite (sample NN54). (d) Granular magnetite type B grains. Note absence of zonation (sample NN59).

and –0.047‰. The $\delta^{18}O$ ± 2σ values for actinolite are 8.16 ± 0.15 and 8.14 ± 0.15‰. The δD ± 2σ values for actinolite from Mina Justa are –35.2 ± 1.86 and –43.14 ± 1.86‰ (Table 4). The water content (wt % H_2O) of the same actinolite samples is 2.03 and 2.24 wt %.

Copper isotope compositions of sulfide separates

Copper isotope data are summarized in Table 4. The δ^{65} Cu values for sulfides from Mina Justa range between -0.32 ± 0.08 and $-0.09 \pm 0.08\%$, with the most negative values coming from samples that present covellite replacing chalcopyrite (Fig. 5d) or symplectitic bornite-chalcocite intergrowths (Fig. 5e).

Discussion

Evolution of the Mina Justa deposit

The magnetite in the manto and the hydrothermal unit corresponds to two separate events as supported by the paragenesis and Ar/Ar geochronology reported by Chen et al. (2010). Those authors associate the magnetite of the manto with the early stage of alteration in Mina Justa (stage 1) and relate it

to the magnetite mineralization at the nearby Marcona IOA deposit, showing it is older than the hydrothermal unit and Cu mineralization. The geochemical and textural characteristics of the magnetite from Mina Justa allow us to identify two generations of magnetite in the deposit. Magnetite with inclusions (type I), found only in the manto, has the highest concentrations of trace elements (V, Ti, Si, Ni, Mn, Mg, Cr, and Ca) in Mina Justa (Fig. 9). As the amount of trace elements that magnetite can host in its structure increases with temperature, magnetite type I is interpreted to have formed at a higher temperature than magnetite from the second generation (types D and B). This is consistent with the temperature estimations from the Mg content in magnetite, where type I yields a higher average temperature than types B and D (Fig. 10). Magnetite with characteristics similar to type I has been described in other IOA deposits in Chile (e.g., Los Colorados; Knipping et al., 2015b), and the estimated temperature for magnetite type I at Mina Justa is consistent with estimations for hydrothermal magnetite formation from other Chilean IOA deposits (Bilenker et al., 2016; Rojas et al., 2018; Salazar et al., 2019; Rodriguez-Mustafa et al., 2020) and with the estimations for magnetite from the Marcona IOA deposit

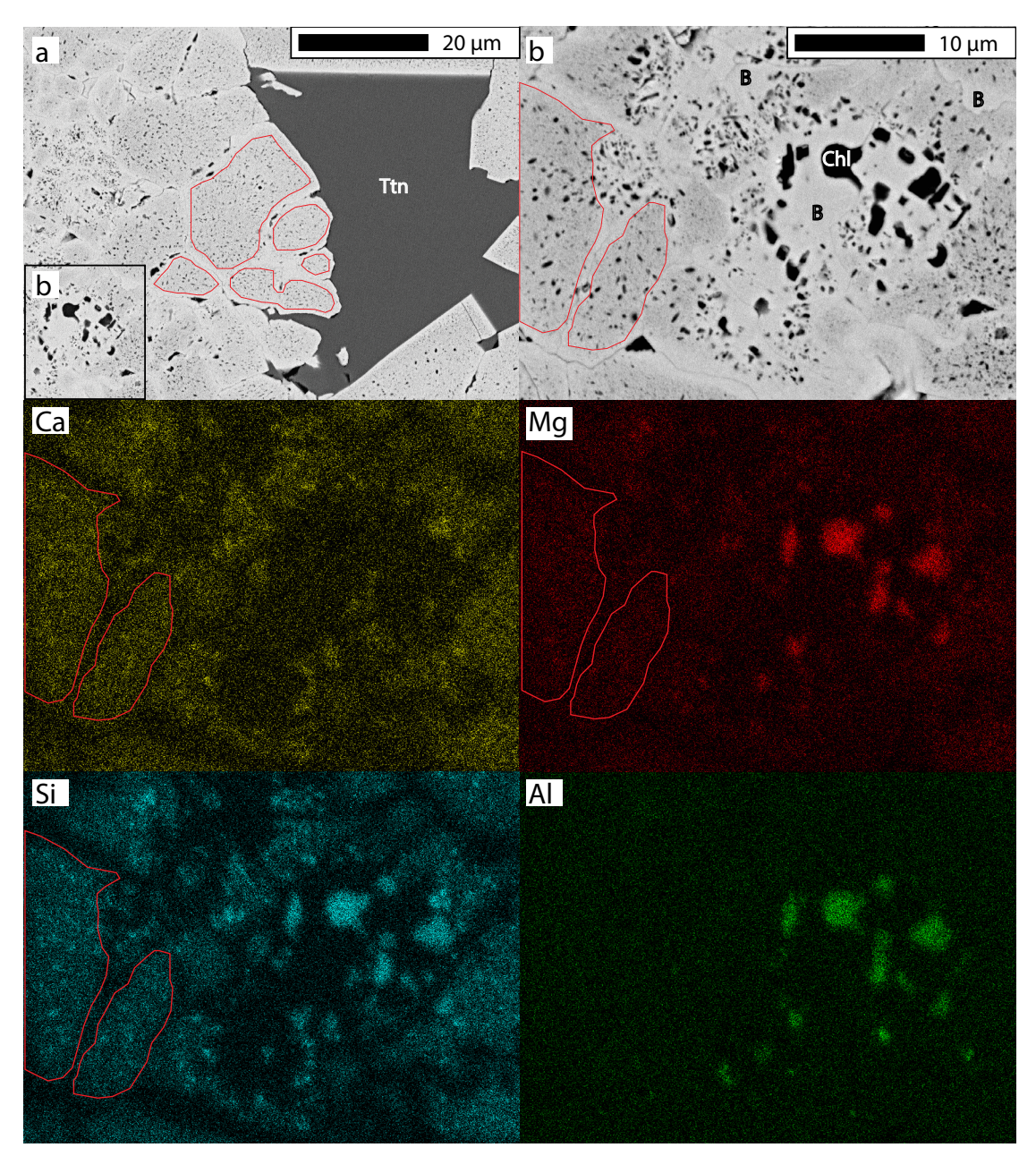


Fig. 8. (a) Magnetite type I cores outlined in red are surrounded by type B magnetite rims that are in contact with interstitial titanite (Ttn). (b) Inset from Fig. 8a showing chloritized actinolite (Chl) intergrown with magnetite type B; note that the left side of 8b is outside and to the left of the lower left box in 8a. The elemental maps are from the same area as Fig. 8b and show that magnetite type I (outlined in red) is enriched in Si, Ca, and Mg compared to magnetite type B.

(Chen et al., 2011). We do not see the high-temperature magnetite (type I) in the hydrothermal unit, only in the manto. If the manto had been emplaced in its current position after the hydrothermal unit had formed, we would see this magnetite type in both geologic units. Therefore, magnetite type I represents the high-temperature first generation of magnetite that formed the manto at Mina Justa.

Stage 2 specular hematite formed along the Mina Justa fault system from a more oxidized fluid (above the hematite-magnetite redox buffer), driven by the sulfur buffer (SO_2 - H_2S - H_2SO_4), and was later reduced as it cooled to form pyrite and stage 3 mushketovite (Giggenbach, 1987; Einaudi et al., 2003;

de Haller and Fontboté, 2009), causing a volume decrease reflected in the porosity of this mineral (Fig. 7a; Hu et al., 2020). Hu et al. (2020) also assigned the formation of granular magnetite to that stage. We found stage 3 mushketovite and granular magnetite in the hydrothermal unit and in the manto, suggesting that the fluids responsible for stages 2 and 3 also flowed through existing fractures associated with the manto.

The fluid responsible for stage 3 precipitated the second generation of magnetite (types D and B) and pyrite. In the manto, this fluid reacted and equilibrated with magnetite type I (as demonstrated by annealing textures such as triple

Table 3: Summary Statistics of Electron Probe Microanalysis (EPMA) Magnetite Data and Temperature Estimations from Mg Content

	Fe	Al	Ca	Si	Mg	Mn	Ti	V	Ni	Cr	О	Total	T_{avg}
Manto ($n = 78$)												
mean	70.71	0.05	0.08	0.19	0.05	0.09	0.06	0.96	0.01	0.03	21.12	93.35	438
std	1.10	0.04	0.16	0.38	0.10	0.03	0.04	0.17	0.01	0.01	0.51	1.29	104
min	68.09	BDL	BDL	BDL	BDL	0.03	BDL	0.67	BDL	0.02	20.01	89.17	372
median	70.82	0.04	0.01	0.02	0.01	0.08	0.05	0.92	0.01	0.03	21.10	93.73	393
max	72.13	0.23	0.67	1.47	0.37	0.18	0.18	1.24	0.02	0.05	22.56	95.58	707
Hyd. unit ($n =$	162)												
mean	71.78	0.09	0.08	0.25	0.05	0.05	0.04	0.21	0.01	0.01	21.13	93.68	478
std	0.83	0.08	0.10	0.29	0.05	0.02	0.03	0.19	0.01	0.01	0.36	0.89	84
min	69.73	0.01	BDL	20.11	90.06	371							
median	71.96	0.05	0.03	0.18	0.02	0.04	0.03	0.14	BDL	BDL	21.11	93.77	459
max	73.55	0.41	0.47	1.23	0.23	0.11	0.16	0.89	0.05	0.05	22.07	95.06	657
Type I $(n = 8)$													
mean	69.10	0.11	0.41	0.97	0.22	0.10	0.11	1.05	0.01	0.04	21.93	94.06	628
std	1.22	0.06	0.19	0.55	0.15	0.03	0.06	0.15	0.00	0.01	0.65	1.06	95
min	68.09	0.03	0.09	0.11	0.02	0.04	BDL	0.88	BDL	0.03	20.95	92.16	459
median	68.61	0.11	0.44	1.25	0.28	0.10	0.14	1.06	0.01	0.04	22.21	94.35	677
max	71.06	0.23	0.67	1.47	0.37	0.14	0.17	1.24	0.02	0.05	22.56	95.58	707
Type D $(n = 37)$	7)												
mean	70.47	0.16	0.19	0.54	0.11	0.05	0.05	0.29	0.01	0.01	21.28	93.14	543
std	1.12	0.11	0.16	0.41	0.08	0.03	0.04	0.32	0.01	0.01	0.70	1.84	106
min	68.20	0.03	BDL	20.01	89.17	373							
median	70.40	0.15	0.17	0.55	0.12	0.05	0.05	0.15	BDL	BDL	21.51	93.98	590
max	72.48	0.41	0.66	1.38	0.36	0.11	0.16	1.11	0.03	0.04	22.42	94.91	705
Type B (n = 19	05)												
mean	71.71	0.06	0.04	0.14	0.03	0.06	0.04	0.46	0.01	0.02	21.07	93.64	443
std	0.78	0.05	0.07	0.20	0.04	0.03	0.03	0.39	0.01	0.01	0.26	0.79	74
min	69.52	BDL	20.15	90.34	371								
median	71.83	0.04	0.01	0.04	0.01	0.05	0.03	0.31	0.01	0.01	21.08	93.74	422
max	73.55	0.36	0.39	1.06	0.27	0.18	0.18	1.24	0.05	0.05	22.02	95.06	671

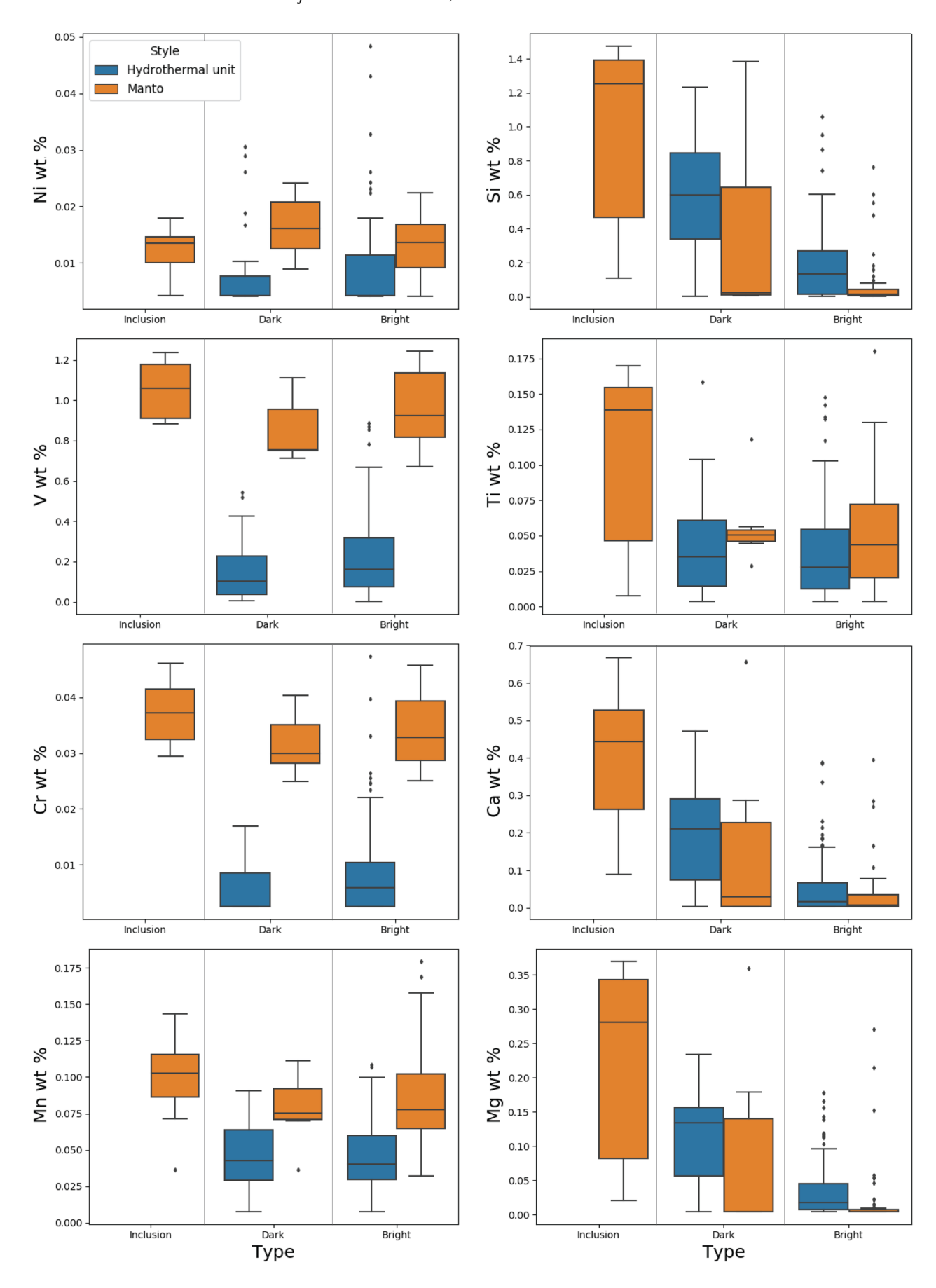
Notes: All concentrations in wt %; oxygen content is stoichiometrically calculated; Hyd. unit = hydrothermal unit, T_{avg} = average temperature in °C estimated from Mg content in magnetite, n = number of points analyzed, BDL = below detection limit

junctions in type B magnetite that is surrounding type I grains; Fig. 6b-c) and precipitated types B and D that contain higher concentrations of V, Ni, Cr, and Mn compared to the same magnetite types in the hydrothermal unit. Those elements are highly compatible in magnetite, whereas Ti, Ca, Si, and Mg formed interstitial titanite and chloritized actinolite (Fig. 8). The significant differences in the concentrations of V, Mn, and Cr clearly discriminate magnetite associated with the manto from magnetite from the hydrothermal unit (Fig. 9).

Type D magnetite is equivalent to types T_{M1-2} (mushketovite) and T_{M2-1} (granular magnetite) described by Hu et al. (2020), while type B magnetite is equivalent to types T_{M1-3} (mushketovite) and T_{M2-2} (granular magnetite) described by

those authors. Magnetite type D enrichment in Si, Mg, and Ca when compared to type B (Fig. 9) suggests that magnetite type D precipitated from the hydrothermal fluid at a higher temperature than magnetite type B, as indicated by the lower concentrations of those elements in magnetite B. The estimations of magnetite formation temperature based on its Mg content suggest that type D precipitated from the fluid at around 550°C, while type B precipitated at around 450°C. These temperatures suggest precipitation from a cooling fluid for these magnetite types, as suggested by Hu et al. (2020) for their equivalent magnetite types. Our estimations are also consistent with magnetite temperatures reported by Chen et al. (2011) for that same stage based on oxygen isotope thermometry and are comparable to magnetite formation temperatures

Fig. 9. Box and whisker plots showing the trace element concentrations of the different magnetite types (Inclusion, Dark, Bright) at Mina Justa. The box comprises the interquartile range (IR), where the horizontal line corresponds to the median. The whiskers extend for 1.5 times the IR from the first and third quartiles. When a significant amount of the data is at the detection limit, the first quartile and the median are the same. The diamonds represent outliers. The color indicates if magnetite belongs to the hydrothermal unit (blue) or to the manto (orange). The manto magnetite is overall enriched in Ni, V, Cr, and Mn when compared to the hydrothermal unit magnetite. Magnetite with inclusions (type I) has the highest concentrations of Si, Ti, Ca, and Mg, followed by magnetite type Dark (D), whereas magnetite type Bright (B) is depleted in the same elements.



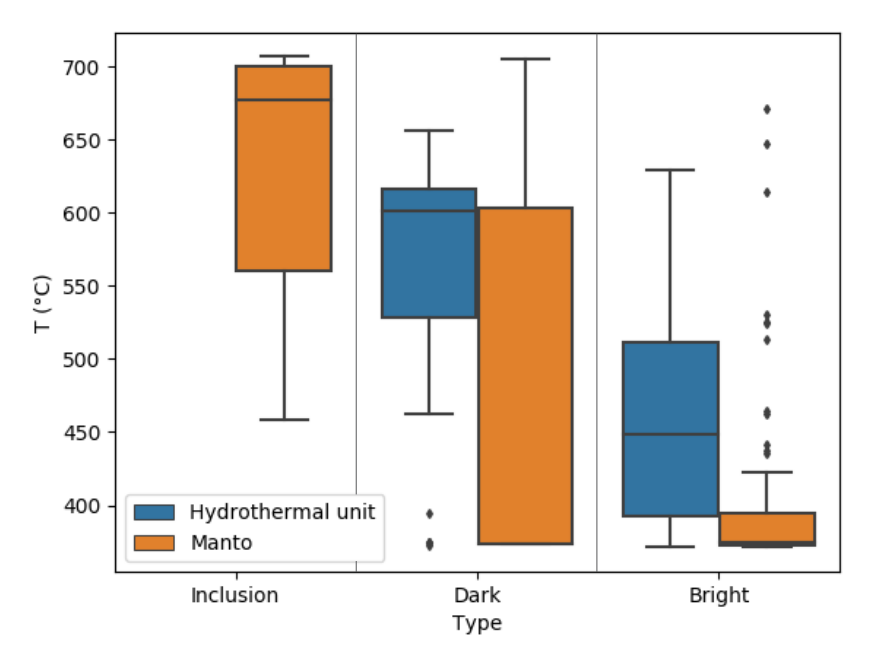


Fig. 10. Box and whisker plots of the crystallization temperature estimations of the different magnetite types (Inclusion, Dark, Bright) for the manto (orange) and the hydrothermal unit (blue) at Mina Justa. The box comprises the interquartile range (IR), where the horizontal line corresponds to the median. The whiskers extend for 1.5 times the IR from the first and third quartiles. The diamonds represent outliers. Magnetite with inclusions (type I) found only in the manto has the highest median temperature, while type Bright (B) has the lowest in the manto and in the hydrothermal unit.

from the Candelaria IOCG deposit in Chile (e.g., Marschik and Fontboté, 2001; Rodriguez-Mustafa et al., 2020).

Stage 4 fluid flowed through the same conduits as stage 3 fluid and precipitated the Cu-sulfides, mostly in the hydrothermal unit and, to a lesser extent, in the manto. This is supported by the similarity between the Cu mineralization assemblage in the hydrothermal unit and the manto and by the proportionality between Cu content and amount of stage 3 magnetite (Sillitoe, 2002). The symplectitic texture between

chalcocite and bornite (Fig. 5e) has also been observed at the Olympic Dam (Roberts and Hudson, 1983; Ciobanu et al., 2017) and Salobo (de Melo et al., 2017) IOCG deposits. This texture is a result of exsolution from an initial bornite-chalcocite solid solution (Bn_{ss}) and is not indicative of a particular temperature or cooling rate (Brett, 1964). A close examination of the phase diagrams in the Cu-Fe-S system indicates that the Bn_{ss} is stable between 300° and 700°C and exsolves into distinct phases ≤ 300 °C under hydrothermal conditions

Table 4: Stable Isotope Results for Magnetite (Fe, O), Actinolite (O, H), and Sulfides (Cu)

Magnetite												Sulfides	
Sample	Style	$\delta^{18}{ m O}$	2sd	$\delta^{56}{ m Fe}$	2sd	n56	$\delta^{17}{ m O}$	$\delta^{18}{ m O}$	$\Delta^{'17}O$	1sd	n	$\delta^{65}\mathrm{Cu}$	2sd
NN51	Manto											-0.25	0.08
NN50	Manto	2.65	0.15	0.19	0.01	3							
NN52	Manto	2.41	0.15	0.24	0.04	3	0.701	1.464	-0.076	0.023	4		
NN04	Manto	2.57	0.15	0.3	0.07	5	1.175	2.305	-0.048	0.006	5		
NN56	Manto	3.16	0.15	0.17	0.03	3							
NN02	Hyd. unit											-0.09	0.08
NN53	Hyd. unit											-0.26	0.08
NN03	Hyd. unit	2.39	0.15	0.35	0.1	5						-0.30	0.08
NN06	Hyd. unit	0.74	0.15	0.4	0.1	6	0.277	0.621	-0.052	0.017	5	-0.32	0.08
GM14	Hyd. unit	1.93	0.15	0.3	0.06	3						-0.11	0.08
GM13	Hyd. unit	1.97	0.15	0.28	0.05	6	0.738	1.505	-0.060	0.018	6		
NN57	Hyd. unit	1.89	0.15	0.28	0.03	3							
Actinolite													
Sample	Style	$\delta^{18}{ m O}$	2sd	$\delta { m D}$	2sd	$_{\mathrm{H_2O}}$							
NN15	Hyd. unit	8.16	0.15	-35.15	1.86	2.03							
NN58	Hyd. unit	8.14	0.15	-43.14	1.86	2.24							

Notes: Isotope values in % with respect to the standard IRMM-14 for Fe, Vienna standard mean ocean water (VSMOW) for O and H, and NIST 976 for Cu; H_2O in wt %; Hyd. unit = Hydrothermal unit; sd = Standard deviation

(Yund and Kullerud, 1966; Sugaki et al., 1975). In the Cu-Fe-S-O system, the assemblage bornite-chalcocite-hematite is stable at 500°C and 1 kbar (Hemley et al., 1992). Additionally, the outward zonation of the hypogene sulfides (bornite, chalcocite \rightarrow chalcopyrite, bornite \rightarrow chalcopyrite > pyrite) combined with the progressive replacement of chalcopyrite by bornite and later by chalcocite (Fig. 5b-c) is consistent with a cooling fluid between ~600° and ~100°C and log aS₂ (S activity coeff) –1 to –15 (Barton, 1970; Einaudi et al., 2003). Therefore, the hypogene sulfides at Mina Justa formed by a stage 4 fluid that precipitated chalcopyrite followed by Bn_{ss} and hematite at high temperature (~500°C). As the Bn_{ss} cooled down to 300°C, it exsolved and generated the symplectitic texture between chalcocite and bornite, which supports a hypogene origin for chalcocite in the deposit.

The temperatures indicated by the sulfide phase assemblage for stage 4 at Mina Justa are consistent with the estimations for similar sulfide mineralization at other IOCG deposits. Based on detailed textural and chemical analysis of similar sulfide assemblages, Ciobanu et al. (2017) concluded that at Olympic Dam, the $\rm Bn_{ss}$ formed at temperatures over 300°C and cooled to below 120°C. Marschik and Fontboté (2001) presented fluid inclusion and sulfide-sulfate fractionation data to establish a temperature of mineralization of 340° to >470°C for the sulfide (pyrite-chalcopyrite) stage at the Candelaria IOCG deposit in Chile. The temperature range reported by those authors is consistent with the zonation of sulfides in Mina Justa, with sulfides crystallizing from a cooling fluid between ~500° and ~300°C.

Chen et al. (2011) used fluid inclusions in calcite veins that crosscut stage 1 to infer a temperature range of 88° to 220°C for the Cu sulfide mineralization (stage 4). However, those inclusions are of unknown origin and could be secondary. We also found late-stage quartz-calcite veins that crosscut stage 4 that must be younger than the Cu mineralization (Fig. 4e); thus, the veins and temperatures reported by Chen et al. (2011) could also be part of this late stage. Temperatures from fluid inclusions in late-stage calcite in the Mantoverde (Rieger and Marschik, 2012) and Candelaria IOCG deposits (Marschik and Fontboté, 2001) are 250°C and ≤236°C, respectively, and are consistent with the temperatures reported by Chen et al. (2011) for Mina Justa.

Source of fluids and metals

The source of the ore fluids and metals remains one of the most controversial aspects in IOCG systems. Hypotheses cover a diverse range of ideas, with some arguing that the metals are sourced from the host rock and mobilized by basinal brines (Barton and Johnson, 1996; Haynes, 2000; Benavides et al., 2007), others favoring a magmatic source for the metals and the fluids (Pollard, 2006), and others supporting a combination of magmatic and basinal fluids (Hitzman et al., 1992; Hitzman, 2000; Chiaradia et al., 2006; Groves et al., 2010; Rieger and Marschik, 2012). Traditional stable isotope systems (H, C, O, S) have been widely used to assess the source of ore fluids. However, nontraditional, stable transition metals isotope systems (i.e., Cu, Fe, Zn, Ag) offer a direct tool to determine the origin of the metals themselves.

A global compilation of stable Fe and O isotope data from IOA deposits and igneous rocks has constrained a field for

magmatic and high-temperature, magmatic-hydrothermal magnetite (Troll et al., 2019). All the Fe-O isotope pairs from the samples from Mina Justa fall within the magmatic and magmatic-hydrothermal field and fingerprint a magmatic/ magmatic-hydrothermal source for the magnetite and mushketovite in the deposit (Fig. 11). The $\delta^{18} \bar{\mathrm{O}}$ values reported here for magnetite from Mina Justa are also consistent with the range (2.7–4.7%) reported by Chen et al. (2011), within the range for magmatic and magmatic-hydrothermal magnetite (Taylor, 1968; Troll et al., 2019). The overall higher δ^{18} O values of magnetite from the manto compared to the hydrothermal unit are consistent with cooling and with a greater proportion of O being sourced from the wall rock, as the manto magnetite replaced carbonate-rich horizons from the Río Grande Formation (Hawkes et al., 2002; Sillitoe, 2002). At the Candelaria IOCG deposit in Chile, magnetite that replaced carbonate-bearing layers also yields elevated $\delta^{18}{
m O}$ values (Rodriguez-Mustafa et al., 2020). Those authors calculated a rock/water volume ratio of 0.2 to 0.3 that resulted in the hydrothermal fluid from which such magnetite precipitated. The higher δ^{56} Fe values in the hydrothermal unit indicate that there was more fractionation than in the manto, indicating that magnetite formed at a lower temperature in the hydrothermal unit, consistent with the temperature estimations from the Mg content of magnetite. The δ^{18} O values for actinolite from the Mina Justa hydrothermal unit overlap the δ^{18} O values reported for actinolite from the Quince IOĀ prospect in Chile (Rodriguez-Mustafa et al., 2020) and the Murdie Murdie IOCG prospect in the Olympic Dam district in Australia (Bastrakov et al., 2007), and are also consistent with a magmatic source.

In order to assess the possible role of meteoric water or basinal brines as oxygen source reservoirs, the calculated $\Delta^{'17}$ O values for magnetite from the manto and the hydrothermal unit at Mina Justa are plotted against their respective δ^{18} O values (Pack et al., 2016; Zakharov et al., 2019; Peters et al., 2020) and compared with data from the El Laco IOA deposit in Chile (Childress et al., 2020) and the Bafq and Sirjan IOA deposits in Iran (Peters et al., 2020; Fig. 11). Our data do not overlap the fields modeled by Peters et al. (2020) for magnetite in equilibrium with seawater (150°-600°C) or meteoric water (400°C); they mostly coincide with the field for magmatic and magmatic-hydrothermal magnetite, indicating a magmatic or magmatic-hydrothermal reservoir for oxygen incorporated into magnetite, consistent with the Fe isotope data. Peters et al. (2020) calculated the isotopic composition of end member magnetite that had equilibrated at high temperature (~800°C) with fluids that had exchanged oxygen with sulfate from evaporites. They interpret the variable $\Delta^{'17}O$ values in their data to indicate that magnetite crystallized from a magmatic fluid that had interacted with evaporites. The data reported here for Mina Justa magnetite do not show such a range in $\Delta^{'17}$ O space (Fig. 11), precluding a considerable input from evaporitic sources in the oxygen reservoir for magnetite. Overall, the O isotopes from Mina Justa support a magmatic or magmatic-hydrothermal reservoir and disallow the predominance of meteoric, seawater, and basinal brines as oxygen sources for magnetite.

Published S isotope data for pyrite from stage 3 (δ^{34} S range from -0.5 to 6.4%) and chalcopyrite from stage 4 (δ^{34} S range

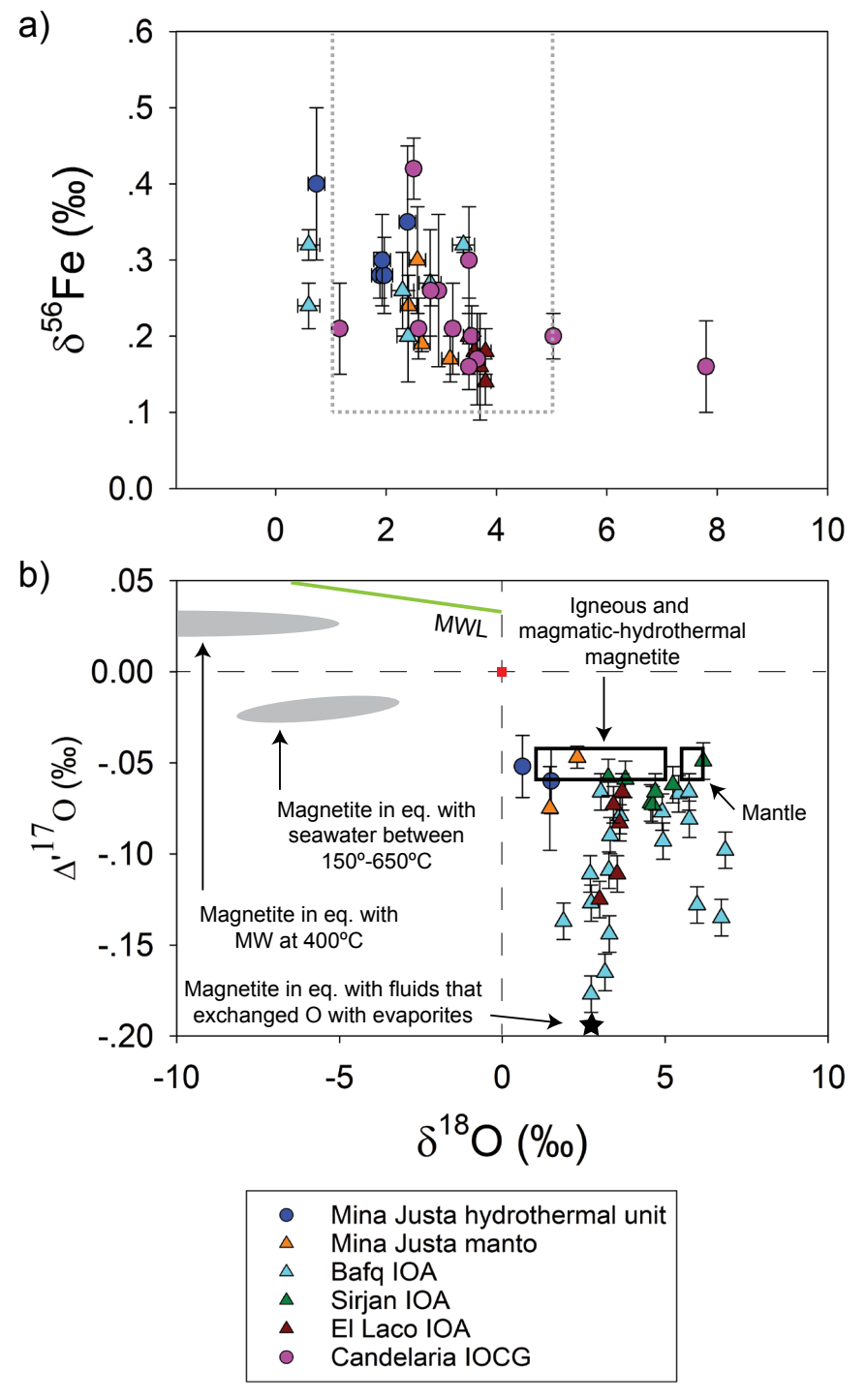


Fig. 11. (a) Scatter plot of δ^{18} O vs. δ^{56} Fe values for magnetite from Mina Justa and other IOCG (circles) and IOA (triangles) deposits. The dashed gray outline defines the field for magnatic and magnatic-hydrothermal magnetite (Taylor, 1968; Troll et al., 2019). Only one data point from Mina Justa is outside of the range for δ^{18} O, but all values are within the range for δ^{56} Fe. Some of the error bars for the δ^{18} O measurements are smaller than the symbol size. (b) Plot of δ^{18} O vs. Δ^{17} O values for magnetite from Mina Justa compared to data from the Bafq, Sirjan, and El Laco IOA deposits (Childress et al., 2020; Peters et al., 2020). The error bars for the δ^{18} O measurements are smaller than the symbol size. The red square marks the values for seawater and the green line shows the Meteoric Water Line (Luz and Barkan, 2010; Sharp et al., 2018). The magnatic and magnatic-hydrothermal magnetite and mantle fields are based on data from Taylor (1968), Pack et al. (2016), Sharp et al. (2018), Troll et al. (2019), Miller et al. (2020), and Peters et al. (2020). The gray ellipses and the black star are from Peters et al. (2020). The star indicates the end-member magnetite that equilibrated at high temperature (~800°C) with fluids that had exchanged oxygen with sulfate from evaporites (Peters et al., 2020). The data from Mina Justa fall within error in the magnatic and magnatic-hydrothermal magnetite box and do not overlap the fields for magnetite in equilibrium with meteoric or seawater. Abbreviations: eq.=equilibrium, MW=Meteoric water, MWL=Meteoric water line.

from –0.6 to 4.6‰) from Mina Justa cluster around 1‰ and show a slight bimodal distribution (Li et al., 2018). Those authors suggested that the stage 3 fluids were mainly of magmatic origin with a later incursion of an external fluid and acknowledged the possibility of a magmatic-hydrothermal source for the S in the chalcopyrite from stage 4 (Li et al., 2018).

The new δ^{65} Cu data reported here, which range from -0.09to -0.32%, are close to the bulk silicate Earth δ ⁶⁵Cu average $(0.06 \pm 0.20 \text{ [2SD]}; \text{Liu et al., } 2015)$ and are within the range for hypogene sulfides in porphyry copper deposits (Fig. 12; Mathur et al., 2009, 2012; Cooke et al., 2014). Thus, the δ ⁶⁵Cu values for sulfides from Mina Justa corroborate the hypogene nature of the chalcopyrite, bornite, and chalcocite, and are consistent with an igneous source for Cu. The two samples with the lowest Cu isotope values from the Mina Justa hydrothermal unit present chalcopyrite being replaced by covellite (Fig. 5d), which is a typical weathering product (Craig and Vaughan, 1994). Such an oxidative process evidenced by the considerable amount of Cu oxides at Mina Justa would cause a loss of heavy Cu isotopes, resulting in a shift to lower δ^{65} Cu values in the original hypogene sulfides (chalcopyrite, bornite, and chalcocite; Mathur et al., 2012).

Conclusions

The study of magnetite from the manto and the hydrothermal unit at the Mina Justa IOCG deposit revealed two generations of Fe oxides that predate the Cu mineralization. Magnetite from the first generation is found in the manto only, and its high trace element content indicates a high temperature of crystallization and is consistent with geochemistry of magnetite from IOA deposits in Chile. Magnetite from the second generation is found mainly in the structurally controlled hydrothermal unit but is also present in the manto. It

consists of mushketovite and granular magnetite and yields lower crystallization temperatures than magnetite from the first generation. The Cu mineralization is hosted mainly in the hydrothermal unit and its zonation in the deposit, along-side with its mineral textures, is consistent with a cooling fluid. The temperature estimations coupled with the novel $\Delta^{\rm 17}{\rm O}$ isotope results disallow the input of significant meteoric or basinal brines as ore fluids. Our Fe, O, and Cu isotope data are consistent with published O and S data and fingerprint a magmatic-hydrothermal source for the ore fluids and metals in the deposit.

Mina Justa is a multistage mineral deposit that records an older IOA mineralization hosted in the manto orebodies that could be related to the neighboring Marcona IOA deposit. The manto bodies at Mina Justa were overprinted by structurally controlled IOCG mineralization (hydrothermal unit) consisting of an initial Fe stage (hematite to magnetite/mush-ketovite + pyrite) and a following Cu sulfide stage. This paragenetic sequence from oxidized to reduced assemblages has been reported at other IOCG deposits in the Andean belt (Marschik and Fontboté, 2001; de Haller and Fontboté, 2009; del Real et al., 2018) and results from the interaction and cooling of the oxidized magmatic-hydrothermal ore fluid with the reduced volcanosedimentary host lithologies (Giggenbach, 1987; de Haller and Fontboté, 2009).

Acknowledgments

M.A.R.M. thanks MARCOBRE S.A., the Society of Economic Geologists Foundation, and the University of Michigan for providing funding. A.C.S. acknowledges funding from the NSF EAR grant #1924192. IB acknowledges support from the NSF EAR grant #1822977. The authors thank Dominique Weis for access to the Pacific Center for Isotopic and Geochemical Research (PCIGR) labs at the University of British

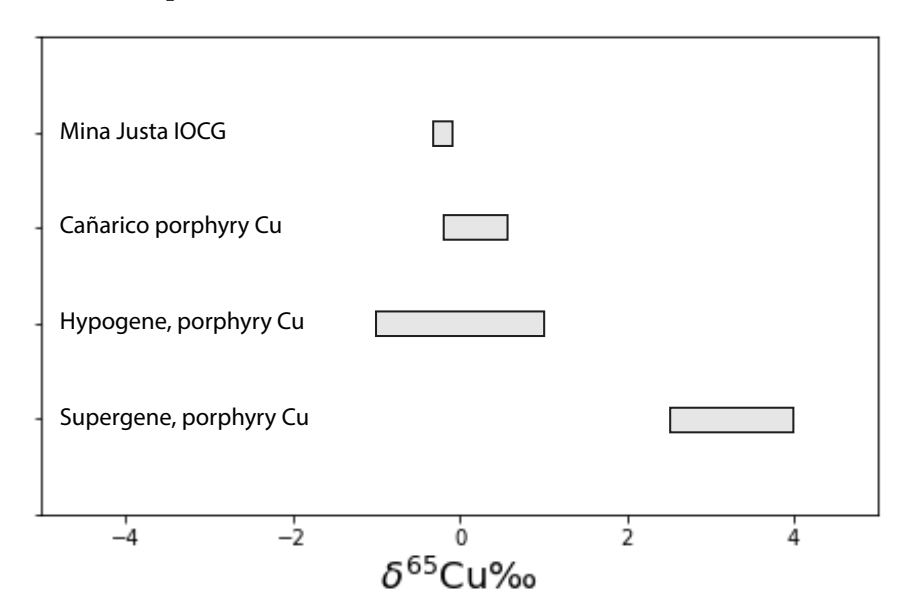


Fig. 12. Ranges of δ^{65} Cu values from sulfides from porphyry copper deposits and the Mina Justa IOCG deposit. The data from Mina Justa is within the range for hypogene sulfides reported for several porphyry Cu deposits and overlaps the range for sulfides from the Cañarico porphyry Cu deposit in northern Peru. Supergene data from the Morenci and El Salvador porphyry deposits from Mathur et al. (2012) and references therein. Hypogene data from the Silver Bell, Chuquicamata, El Salvador, and Morenci porphyry deposits from Mathur et al. (2009). Cañarico data from Mathur et al. (2012). Mina Justa data from this study.

Columbia, and the Mine Geology and Exploration teams and support staff at Mina Justa for assistance and support during and after the field visit. The authors also thank reviewers Antoine de Haller and Martin Smith, Associate Editor Lucas Marshall, Editor Larry Meinert, and two other members of the editorial board for their constructive comments that contributed to improve this manuscript considerably.

REFERENCES

- Atkin, B.P., Injoque, J., and Harvey, P.K., 1985, Cu-Fe amphibole mineralization in the Arequipa segment, *in* Pitcher, W.S., Atherton, M.P., Cobbing, E.J., and Beckinsale, R.D., eds., Magmatism at the plate edge: The Peruvian Andes: Glasgow, UK, Blackie, p. 261–270.
- Barra, F., Reich, M., Selby, D., Rojas, P., Simon, A., Salazar, E., and Palma, G., 2017, Unraveling the origin of the Andean IOCG clan: A Re-Os isotope approach: Ore Geology Reviews, v. 81, p. 62–78.
- Barton, M.D., 2014, Iron oxide(-Cu-Au-REE-P-Ag-U-Co) systems, in Holland, H.D., and Turekian, K.K., eds., Treatise on geochemistry, 2nd ed.: Oxford, Elsevier, p. 515–541.
- Barton, M.D., and Johnson, D.A., 1996, An evaporitic-source model for igneous-related Fe oxide(-REE-Cu-Au-U) mineralization: Geology, v. 24, p. 259–262.
- Barton, P.B., Jr., 1970, Sulfide petrology: Mineralogical Society of America, v. 3, p. 187–198.
- Bastrakov, E.N., Skirrow, R.G., and Davidson, G.J., 2007, Fluid evolution and origins of iron oxide Cu-Au prospects in the Olympic Dam district, Gawler craton, South Australia: Economic Geology, v. 102, p. 1415–1440.
- Benavides, J., Kyser, T.K., Clark, A.H., Oates, C.J., Zamora, R., Tarnovschi, R., and Castillo, B., 2007, The Mantoverde iron oxide-copper-gold district, III Región, Chile: The role of regionally derived, nonmagmatic fluids in chalcopyrite mineralization: Economic Geology, v. 102, p. 415–440.
- Bilenker, L.D., Simon, A.C., Reich, M., Lundstrom, C.C., Gajos, N., Bindeman, I., Barra, F., and Munizaga, R., 2016, Fe-O stable isotope pairs elucidate a high-temperature origin of Chilean iron oxide-apatite deposits: Geochimica et Cosmochimica Acta, v. 177, p. 94–104.
- Bindeman, I.N., Kamenetsky, V.S., Palandri, J., and Vennemann, T., 2012, Hydrogen and oxygen isotope behaviors during variable degrees of upper mantle melting: Example from the basaltic glasses from Macquarie Island: Chemical Geology, v. 310–311, p. 126–136.
- Bindeman, I.N., Zakharov, D.O., Palandri, J., Greber, N.D., Dauphas, N., Retallack, G.J., Hofmann, A., Lackey, J.S., and Bekker, A., 2018, Rapid emergence of subaerial landmasses and onset of a modern hydrologic cycle 2.5 billion years ago: Nature, v. 557, p. 545–548.
- Brett, R., 1964, Experimental data from the system Cu-Fe-S and their bearing on exsolution textures in ores: Economic Geology, v. 59, p. 1241–1269.
- Caldas Vidal, J., 1978, Geología del cuadrángulo de San Juan, Acarí y Yauca 31-m, 31-n, 32-n [Boletín A 30]: Instituto Geológico, Minero y Metalúrgico INGEMMET.
- Canil, D., and Lacourse, T., 2020, Geothermometry using minor and trace elements in igneous and hydrothermal magnetite: Chemical Geology, v. 541, article 119576.
- Chen, H., Clark, A.H., Kyser, T.K., Ullrich, T.D., Baxter, R., Chen, Y., and Moody, T.C., 2010, Evolution of the giant Marcona-Mina Justa iron oxide-copper-gold district, south-central Peru: Economic Geology, v. 105, p. 155–185.
- Cĥen, H., Kyser, T.K., and Clark, A.H., 2011, Contrasting fluids and reservoirs in the contiguous Marcona and Mina Justa iron oxide-Cu (-Ag-Au) deposits, south-central Perú: Mineralium Deposita, v. 46, p. 677–706.
- Chiaradia, M., Banks, D., Cliff, R., Marschik, R., and de Haller, A., 2006, Origin of fluids in iron oxide-copper-gold deposits: Constraints from δ^{37} Cl, 87 Sr/ 86 Sri, and Cl/Br: Mineralium Deposita, v. 41, p. 565–573.
- Childress, T.M., Simon, A.C., Reich, M., Barra, F., Bilenker, L.D., La Cruz, N.L., Bindeman, I.N., and Ovalle, J.T., 2020, Triple oxygen (δ¹8O, Δ¹7O), hydrogen (δ²H), and iron (δ⁵6Fe) stable isotope signatures indicate a silicate magma source and magmatic-hydrothermal genesis for magnetite ore bodies at El Laco, Chile: Economic Geology, v. 115, p. 1519–1536.
- Ciobanu, C.L., Cook, N.J., and Ehrig, K., 2017, Ore minerals down to the nanoscale: Cu-(Fe)-sulphides from the iron oxide copper gold deposit at Olympic Dam, South Australia: Ore Geology Reviews, v. 81, p. 1218–1235.

- Clark, A.H., Farrar, E., Kontak, D.J., Langridge, R.J., Arenas F., M.J., France, L.J., McBride, S.L., Woodman, P.L., Wasteneys, H.A., Sandeman, H.A., and Archibald, D.A., 1990, Geologic and geochronologic constraints on the metallogenic evolution of the Andes of southeastern Peru: Economic Geology, v. 85, p. 1520–1583.
- Cooke, D.R., Hollings, P., Wilkinson, J.J., and Tosdal, R.M., 2014, Geochemistry of porphyry deposits, in Holland, H.D., and Turekian, K.K., eds., Treatise on geochemistry, 2nd ed.: Oxford, Elsevier, p. 357–381.
- Corriveau, L., Montreuil, J.-F., and Potter, E.G., 2016, Alteration facies linkages among iron oxide copper-gold, iron oxide-apatite, and affiliated deposits in the Great Bear magmatic zone, Northwest Territories, Canada: Economic Geology, v. 111, p. 2045–2072.
- Craddock, P.R., and Dauphas, N., 2011, Iron isotopic compositions of geological reference materials and chondrites: Geostandards and Geoanalytical Research, v. 35, p. 101–123.
- Craig, J.R., and Vaughan, D.J., 1994, Ore mineral textures, in Ore microscopy and ore petrography: New York, Wiley, p. 120–163.
- Einaudi, M.T., Hedenquist, J.W., and Inan, E.E., 2003, Sulfidation state of fluids in active and extinct hydrothermal systems: Transitions from porphyry to epithermal environments: Society of Economic Geologists, Special Publication 10, p.285–313.
- Espinoza, S., Veliz, H., Esquivel, J., Arias, J., and Moraga, A., 1996, The Cupriferous province of the Coastal Range, Northern Chile: Society of Economic Geologists, Special Publication 5, p. 19–32.
- Fonseca, A., 2016, Mina Justa 3D model summary report: SRK Consulting. Fowler, A., and Stephenson, P.R., 2016, Mina Justa estimation of mineral resource: AMC Mining Consultants Ltd. 716010.
- Giggenbach, W.F., 1987, Redox processes governing the chemistry of fumarolic gas discharges from White Island, New Zealand: Applied Geochemistry, v. 2, p. 143–161.
- Groves, D.I., Bierlein, F.P., Meinert, L.D., and Hitzman, M.W., 2010, Iron oxide copper-gold (IOCG) deposits through Earth history: Implications for origin, lithospheric setting, and distinction from other epigenetic iron oxide deposits: Economic Geology, v. 105, p. 641–654.
- de Haller, A., and Fontboté, L., 2009, The Raúl-Condestable iron oxide copper-gold deposit, central coast of Peru: Ore and related hydrothermal alteration, sulfur isotopes, and thermodynamic constraints: Economic Geology, v. 104, p. 365–384.
- de Haller, A., Corfu, F., Fontboté, L., Schaltegger, U., Barra, F., Chiaradia, M., Frank, M., and Zúñiga Alvarado, J., 2006, Geology, geochronology, and Hf and Pb isotope data of the Raúl-Condestable iron oxide copper-gold deposit, central coast of Peru: Economic Geology, v. 101, p. 281–310.
- Hawkes, N., 2003, Model for the evolution of mineralisation at Mina Justa and the Marcona district: Rio Tinto, 2 p.
- Hawkes, N., Clark, A.H., and Moody, T.C., 2002, Marcona and Pampa de Pongo: Giant Mesozoic Fe-(Cu, Au) deposits in the Peruvian Coastal Belt, *in* Porter, T.M., ed., Hydrothermal iron oxide copper-gold & related deposits: A global perspective: Adelaide, Porter GeoConsultancy Publishing, p. 115–130.
- Haynes, D.W., 2000, Iron oxide copper (-gold) deposits: Their position in the ore spectrum and modes of origin, *in* Porter, T.M., ed., Hydrothermal iron oxide copper-gold & related deposits: A global perspective: Adelaide, Porter GeoConsultancy Publishing p. 71–90
- Porter GeoConsultancy Publishing, p. 71–90.

 Hemley, J.J., Cygan, G.L., Fein, J.B., Robinson, G.R., and d'Angelo, W.M., 1992, Hydrothermal ore-forming processes in the light of studies in rock-buffered systems; I, Iron-copper-zinc-lead sulfide solubility relations: Economic Geology, v. 87, p. 1–22.
- Hitzman, M.W., 2000, Îron oxide-Cu-Au deposits: What, where, when, and why, in Porter, T.M., ed., Hydrothermal iron oxide copper-gold & related deposits: A global perspective: Adelaide, Porter GeoConsultancy Publishing, p. 9–25.
- Hitzman, M.W., Oreskes, N., and Einaudi, M.T., 1992, Geological characteristics and tectonic setting of proterozoic iron oxide (Cu-U-Au-REE) deposits: Precambrian Research, v. 58, p. 241–287.
- Hu, X., Chen, H., Beaudoin, G., and Zhang, Y., 2020, Textural and compositional evolution of iron oxides at Mina Justa (Peru): Implications for mush-ketovite and formation of IOCG deposits: American Mineralogist, v. 105, p. 397–408.
- Huang, F., Zhang, Z., Lundstrom, C.C., and Zhi, X., 2011, Iron and magnesium isotopic compositions of peridotite xenoliths from Eastern China: Geochimica et Cosmochimica Acta, v. 75, p. 3318–3334.
- Injoque, J., 2002, Fe oxide-Cu-Au deposits in Peru: An integrated view, in Porter, T.M., ed., Hydrothermal iron oxide copper-gold and related

- deposits: A global perspective, v. 2: Adelaide, Porter GeoConsultancy Publishing, p. 97–113.
- Knipping, J.L., Bilenker, L.D., Simon, A.C., Reich, M., Barra, F., Deditius, A.P., Lundstrom, C., Bindeman, I., and Munizaga, R., 2015a, Giant Kirunatype deposits form by efficient flotation of magmatic magnetite suspensions: Geology, v. 43, p. 591–594.
- Knipping, J.L., Bilenker, L.D., Simon, A.C., Reich, M., Barra, F., Deditius, A.P., Wälle, M., Heinrich, C.A., Holtz, F., and Munizaga, R., 2015b, Trace elements in magnetite from massive iron oxide-apatite deposits indicate a combined formation by igneous and magnatic-hydrothermal processes: Geochimica et Cosmochimica Acta, v. 171, p. 15–38.
- Li, R., Chen, H., Xia, X., Yang, Q., Danyushevsky, L.V., and Lai, C., 2018, Using integrated in-situ sulfide trace element geochemistry and sulfur isotopes to trace ore-forming fluids: Example from the Mina Justa IOCG deposit (southern Perú): Ore Geology Reviews, v. 101, p. 165–179.
- Liu, S.-A., Huang, J., Liu, J., Wörner, G., Yang, W., Tang, T.-J., Chen, Y., Tang, L., Zheng, J., and Li, S., 2015, Copper isotopic composition of the silicate Earth: Earth and Planetary Science Letters, v. 427, p. 95–103.
- Loewen, M.W., and Bindeman, I.N., 2016, Oxygen isotope thermometry reveals high magmatic temperatures and short residence times in Yellow-stone and other hot-dry rhyolites compared to cold-wet systems: American Mineralogist, v. 101, p. 1222–1227.
- Luz, B., and Barkan, E., 2010, Variations of ¹⁷O/¹⁶O and ¹⁸O/¹⁶O in meteoric waters: Geochimica et Cosmochimica Acta, v. 74, p. 6276–6286.
- Marschik, R., and Fontboté, L., 2001, The Candelaria-Punta del Cobre iron oxide Cu-Au(-Zn-Ag) deposits, Chile: Economic Geology, v. 96, p. 1799–1826.
- Mathur, R., Titley, S., Barra, F., Brantley, S., Wilson, M., Phillips, A., Munizaga, F., Maksaev, V., Vervoort, J., and Hart, G., 2009, Exploration potential of Cu isotope fractionation in porphyry copper deposits: Journal of Geochemical Exploration, v. 102, p. 1–6.
 Mathur, R., Ruiz, J., Casselman, M.J., Megaw, P., and van Egmond, R., 2012,
- Mathur, R., Ruiz, J., Casselman, M.J., Megaw, P., and van Egmond, R., 2012, Use of Cu isotopes to distinguish primary and secondary Cu mineralization in the Cañariaco Norte porphyry copper deposit, northern Peru: Mineralium Deposita, v. 47, p. 755–762.
- de Melo, G.H.C., Monteiro, L.V.S., Xavier, R.P., Moreto, C.P.N., Santiago, E.S.B., Dufrane, S.A., Aires, B., and Santos, A.F.F., 2017, Temporal evolution of the giant Salobo IOCG deposit, Carajás province (Brazil): Constraints from paragenesis of hydrothermal alteration and U-Pb geochronology: Mineralium Deposita, v. 52, p. 709–732.
- Miller, M.F., Pack, A., Bindeman, I.N., and Greenwood, R.C., 2020, Standardizing the reporting of Δ^{17} O data from high precision oxygen triple-isotope ratio measurements of silicate rocks and minerals: Chemical Geology, v. 532, article 119332.
- Naslund, H.R., Henriquez, F., Nyström, J.O., Vivallo, W., and Dobbs, F.M., 2002, Magmatic iron ires and associated mineralisation: Examples from the Chilean High Andes and Coastal Cordillera, *in* Porter, T.M., ed., Hydrothermal iron oxide copper-gold & related deposits: A global perspective: Adelaide, Porter GeoConsultancy Publishing, p. 207–226.
- Pack, A., Tanaka, R., Hering, M., Sengupta, S., Peters, S., and Nakamura, E., 2016, The oxygen isotope composition of San Carlos olivine on the VSMOW2-SLAP2 scale: Rapid Communications in Mass Spectrometry, v. 30, p. 1495–1504.
- Peters, S.T.M., Alibabaie, N., Pack, A., McKibbin, S.J., Raeisi, D., Nayebi, N., Torab, F., Ireland, T., and Lehmann, B., 2020, Triple oxygen isotope variations in magnetite from iron-oxide deposits, central Iran, record magmatic fluid interaction with evaporite and carbonate host rocks: Geology, v. 48, p. 211–215.
- Pollard, P.J., 2006, An intrusion-related origin for Cu-Au mineralization in iron oxide-copper-gold (IOCG) provinces: Mineralium Deposita, v. 41, p. 179–187.
- QÎ, H., Coplen, T.B., Gehre, M., Vennemann, T.W., Brand, W.A., Geilmann, H., Olack, G., Bindeman, I.N., Palandri, J., Huang, L., and Longstaffe, F.J., 2017, New biotite and muscovite isotopic reference materials, USGS57 and USGS58, for δ^2 H measurements—A replacement for NBS 30: Chemical Geology, v. 467, p. 89–99.
- del Real, I., Thompson, J.F.H., and Carriedo, J., 2018, Lithological and structural controls on the genesis of the Candelaria-Punta del Cobre iron oxide copper gold district, northern Chile: Ore Geology Reviews, v. 102, p. 106–153.

- del Real, I., Thompson, J.F.H., Simon, A.C., and Reich, M., 2020, Geochemical and isotopic signature of pyrite as a proxy for fluid source and evolution in the Candelaria-Punta del Cobre iron oxide copper-gold district, Chile: Economic Geology, v. 115, p. 1493–1518.
- Reich, M., Simon, A.C., Deditius, A.P., Barra, F., Chryssoulis, S., Lagas, G., Tardani, D., Knipping, J., Bilenker, L., Sánchez-Alfaro, P., Roberts, M., and Munizaga, R., 2016, Trace element signature of pyrite from the Los Colorados iron oxide-apatite (IOA) deposit, Chile: A missing link between Andean IOA and IOCG systems?: Economic Geology, v. 111, p. 743–761.
- Rieger, A.A., and Marschik, R., 2012, The evolution of the hydrothermal IOCG system in the Mantoverde district, northern Chile: New evidence from microthermometry and stable isotope geochemistry: Mineralium Deposita, v. 47, p. 359–369.
- Roberts, D.E., and Hudson, G.R.T., 1983, The Olympic Dam copper-uranium-gold deposit, Roxby Downs, South Australia: Economic Geology, v. 78, p. 799–822.
- Rodriguez-Mustafa, M.A., Simon, A.C., del Real, I., Thompson, J.F.H., Bilenker, L.D., Barra, F., Bindeman, I., and Cadwell, D., 2020, A continuum from iron oxide copper-gold to iron oxide-apatite deposits: Evidence from Fe and O stable isotopes and trace element chemistry of magnetite: Economic Geology, v. 115, p. 1443–1459.
- Rojas, P.A., Barra, F., Deditius, A., Reich, M., Simon, A., Roberts, M., and Rojo, M., 2018, New contributions to the understanding of Kiruna-type iron oxide-apatite deposits revealed by magnetite ore and gangue mineral geochemistry at the El Romeral deposit, Chile: Ore Geology Reviews, v. 93, p. 413–435.
- Salazar, E., Barra, F., Reich, M., Simon, A., Leisen, M., Palma, G., Romero, R., and Rojo, M., 2019, Trace element geochemistry of magnetite from the Cerro Negro Norte iron oxide-apatite deposit, northern Chile: Mineralium Deposita.
- Sharp, Z.D., Wostbrock, J.A.G., and Pack, A., 2018, Mass-dependent triple oxygen isotope variations in terrestrial materials: Geochemical Perspectives Letters, v. 7, p. 27–31.
- Sillitoe, R.H., 2002, Implications of sulphide zoning pattern, Mina Justa copper prospect, Marcona project, Southern Peru: Rio Tinto, 9 p.
- ——2003, Iron oxide-copper-gold deposits: An Andean view: Mineralium Deposita, v. 38, p. 787–812.
- Simon, A., Knipping, J., Reich, M., Barra, F., Deditius, A., Bilenker, L., and Childress, T., 2018, A holistic model that combines igneous and magmatic-hydrothermal processes to explain Kiruna-type iron oxide-apatite deposits and iron oxide-copper-gold deposits as products of a single evolving ore system: Society of Economic Geologists, Special Publication 21, p. 89–114.
- Sugaki, A., Shima, H., Kitakaze, A., and Harada, H., 1975, Isothermal phase relations in the system Cu-Fe-S under hydrothermal conditions at 350 degrees C and 300 degrees C: Economic Geology, v. 70, p. 806–823.
- Taylor, H.P., 1968, The oxygen isotope geochemistry of igneous rocks: Contributions to Mineralogy and Petrology, v. 19, p. 1–71.
- Troll, V.R., Weis, F.A., Jonsson, E., Andersson, U.B., Majidi, S.A., Högdahl, K., Harris, C., Millet, M.-A., Chinnasamy, S.S., Kooijman, E., and Nilsson, K.P., 2019, Global Fe-O isotope correlation reveals magmatic origin of Kiruna-type apatite-iron-oxide ores: Nature Communications, v. 10, p. 1712.
- Vidal, C.E., Injoque-Espinoza, J., Sidder, G.B., and Mukasa, S.B., 1990, Amphibolitic Cu-Fe skarn deposits in the central coast of Peru: Economic Geology, v. 85, p. 1447–1461.
- Wasteneys, H.A., Clark, A.H., Farrar, E., and Langridge, R.J., 1995, Grenvillian granulite-facies metamorphism in the Arequipa Massif, Peru: a Laurentia-Gondwana link: Earth and Planetary Science Letters, v. 132, p. 63–73.
- Williams, P., Barton, M.D., Johnson, D.A., Fontboté, L., De Haller, A., Mark, G., Oliver, N.H.S., and Marschik, R., 2005, Iron oxide copper-gold deposits: Geology, space-time distribution, and possible modes of origin: Economic Geology, v. 100, p. 371–405.
- Yund, R.A., and Kullerud, G., 1966, Thermal stability of assemblages in the Cu-Fe-S system: Journal of Petrology, v. 7, p. 454–488.
- Zakharov, D.O., Bindeman, I.N., Tanaka, R., Friòleifsson, G.Ó., Reed, M.H., and Hampton, R.L., 2019, Triple oxygen isotope systematics as a tracer of fluids in the crust: A study from modern geothermal systems of Iceland: Chemical Geology, v. 530, p. 119312.

Maria Alejandra Rodriguez Mustafa is a Ph.D. candidate at the University of Michigan investigating the origin of iron oxide-copper-gold (IOCG) and iron oxide-apatite (IOA) ore deposits. Maria Alejandra earned her B.S. Honors in Geology from the National University of Colombia.

